Am J Physiol Heart Circ Physiol 311: H1470–H1484, 2016.
First published October 7, 2016; doi:10.1152/ajpheart.00500.2016.

Spontaneous initiation of premature ventricular complexes and arrhythmias in type 2 long QT syndrome

Xiaodong Huang,[1,3]* Tae Yun Kim,[4]* Gideon Koren,[4] Bum-Rak Choi,[4] and Zhilin Qu[1,2]

[1]*Department of Medicine (Cardiology), David Geffen School of Medicine, University of California, Los Angeles, California;* [2]*Department of Biomathematics, David Geffen School of Medicine, University of California, Los Angeles, California;* [3]*Department of Physics, South China University of Technology, Guangzhou, China; and* [4]*Division of Cardiology, Cardiovascular Research Center, Rhode Island Hospital, Warren Alpert Medical School of Brown University, Providence, Rhode Island*

Submitted 15 July 2016; accepted in final form 3 October 2016

Huang X, Kim TY, Koren G, Choi BR, Qu Z. Spontaneous initiation of premature ventricular complexes and arrhythmias in type 2 long QT syndrome. *Am J Physiol Heart Circ Physiol* 311: H1470–H1484, 2016. First published October 7, 2016; doi:10.1152/ajpheart.00500.2016.—The occurrence of early afterdepolarizations (EADs) and increased dispersion of repolarization are two known factors for arrhythmogenesis in long QT syndrome. However, increased dispersion of repolarization tends to suppress EADs due to the source-sink effect, and thus how the two competing factors cause initiation of arrhythmias remains incompletely understood. Here we used optical mapping and computer simulation to investigate the mechanisms underlying spontaneous initiation of arrhythmias in type 2 long QT (LQT2) syndrome. In optical mapping experiments of transgenic LQT2 rabbit hearts under isoproterenol, premature ventricular complexes (PVCs) were observed to originate from the steep spatial repolarization gradient (RG) regions and propagated unidirectionally. The same PVC behaviors were demonstrated in computer simulations of tissue models of rabbits. Depending on the heterogeneities, these PVCs could lead to either repetitive focal excitations or reentry without requiring an additional vulnerable substrate. Systematic simulations showed that cellular phase 2 EADs were either suppressed or confined to the long action potential region due to the source-sink effect. Tissue-scale phase 3 EADs and PVCs occurred due to tissue-scale dynamical instabilities caused by RG and enhanced L-type calcium current ($I_{Ca,L}$), occurring under both large and small RG. Presence of cellular EADs was not required but potentiated PVCs when RG was small. We also investigated how other factors affect the dynamical instabilities causing PVCs. Our main conclusion is that tissue-scale dynamical instabilities caused by RG and enhanced $I_{Ca,L}$ give rise to both the trigger and the vulnerable substrate simultaneously for spontaneous initiation of arrhythmias in LQT2 syndrome.

early afterdepolarization; repolarization gradient; premature ventricular complex; initiation of arrhythmias

NEW & NOTEWORTHY

Under type 2 long QT conditions, cellular phase 2 early afterdepolarizations are suppressed by repolarization gradient, but tissue-scale phase 3 early afterdepolarizations occur spontaneously via dynamical instabilities caused by repolarization gradient and enhanced L-type calcium current, resulting in both the trigger and the vulnerable substrate simultaneously for spontaneous initiation of arrhythmias.

PROLONGATION OF ACTION POTENTIAL duration (APD) in long QT syndromes (LQTS) as well as in other cardiac diseases is associated with an increased risk of ventricular arrhythmias, in particular Torsade de Pointes (TdP) (34, 45, 54). Two key factors are closely associated with arrhythmogenesis in LQTS (1, 2, 6, 17, 21, 43, 44, 59, 62, 68): early afterdepolarizations (EADs) and increased dispersion of repolarization. EADs occur during the repolarization phase of the action potential (AP), resulting from increased inward currents and/or decreased outward currents. Dispersion of repolarization exists in the ventricles of normal hearts due to heterogeneous ion channel distributions, which is amplified in LQTS (6, 62). EADs are known to be able to trigger premature ventricular complexes (PVCs) while increased dispersion of repolarization increases the chance of conduction block of a PVC. Therefore, it is natural to assume that an EAD occurring in one region generates a PVC that propagates into another region with a steep repolarization gradient (RG) and is then blocked regionally to initiate arrhythmias in LQTS. However, for an EAD to cause a PVC in tissue, the EAD in the longer APD region must propagate to the adjacent shorter APD region. It is well known that, due to the source-sink effect, increasing RG tends to suppress EADs (22, 66), making it more difficult for EADs to trigger PVCs. Therefore, increased RG and the occurrence of EADs are two competing processes at the tissue scale, but how they interact to promote arrhythmias in LQTS remains unclear.

Whether an EAD can propagate to cause a PVC in structurally normal tissue, such as in LQTS, remains controversial. Damiano and Rosen (13) showed that phase 3 EADs (takeoff potential under −50 mV) can trigger PVCs in Purkinje fibers but phase 2 EADs (takeoff potential over −30 mV) could not. Yan et al. (67) used wedge preparations and intracellular microelectrode recordings to show that phase 2 EADs might propagate from the endocardial layer to the epicardial layer to initiate PVCs and finally lead to TdP, but an increased RG was needed for the phase 2 EADs to induce arrhythmias in rabbit hearts. Supporting the observation that increased RG was required for phase 2 EADs to induce PVCs, Maruyama et al. (32), who used optical mapping of rabbit hearts under E4031 and hypokalemia, observed that when the phase 2 EADs were confined to the center of the long APD region, they could not generate PVCs, but when they occurred near or transmitted to the steep RG region, phase 3 EADs and PVCs were induced and resulted in ectopic excitations or reentry. Other optical mapping studies (23, 27) also showed that PVCs originated spontaneously from the steep RG regions. These experiments seemed to show that increased RG potentiated propagation of

* X. Huang and T. Y. Kim contributed equally to this work.

Address for reprint requests and other correspondence: Z. Qu, Dept. of Medicine, Div. of Cardiology, David Geffen School of Medicine at UCLA, A2-237 CHS, 650 Charles E. Young Dr. South, Los Angeles, CA 90095 (e-mail: zqu@mednet.ucla.edu).

phase 2 EADs into PVCs to initiate arrhythmias in LQTS. This contradicts the commonly held belief that raising the RG increases the sink effect, which suppresses EADs.

In this study, we systematically investigated the roles of EADs and RG in the genesis of PVCs and ventricular arrhythmias in LQT2 syndrome. We hypothesized that PVCs are consequences of a tissue-scale dynamical instability caused by RG and enhanced L-type calcium (Ca) current ($I_{Ca,L}$), not a result of propagation of cellular phase 2 EADs. RG-induced PVCs propagate unidirectionally, which can result in reentrant arrhythmias without requiring an additional tissue substrate. To test this hypothesis, we carried out optical mapping experiments in transgenic LQT2 rabbit hearts and computer simulations of one-dimensional (1D) cable and two-dimensional (2D) tissue using a rabbit ventricular myocyte model. Optical mapping experiments showed that PVCs tended to initiate spontaneously in the steep RG region and propagate unidirectionally. Systematic computer simulations showed that cellular phase 2 EADs (i.e., EADs that occur in isolated single cells) were mostly suppressed or confined to the long APD region due to the source-sink effect. On the other hand, tissue-scale phase 3 EADs (i.e., EADs in tissue but not in isolated cells) could occur in the RG region due to tissue-scale dynamical instabilities, resulting in unidirectionally propagating PVCs. PVCs could occur under either large or small RG depending on the magnitude of $I_{Ca,L}$, while requiring a two- to threefold increase in $I_{Ca,L}$, which is much higher than that required for the occurrence of cellular EADs, but within the physiological range induced by sympathetic stimulation. The presence of cellular phase 2 EADs potentiated RG-mediated tissue-scale phase 3 EAD and PVC formation when the RG was small. Because the PVCs propagated unidirectionally, reentry could form in tissue in the same location where the PVCs were initiated, i.e., the triggers and tissue substrate for arrhythmia initiation originated from the same source: a tissue-scale dynamical instability caused by RG and enhanced $I_{Ca,L}$.

MATERIALS AND METHODS

Optical Mapping Experiments

Transgenic LQT2 rabbits (6) were killed with buprenorphene (0.03 mg/kg im), acepromazine (0.5 mg/kg im), xylazene (15 mg/kg im), ketamine (60 mg/kg im), pentothal (35 mg/kg iv), and heparin (200 U/kg). This investigation conformed to the current *Guide for the Care and Use of Laboratory Animals* published by the National Institutes of Health (NIH Publication No. 85-23, revised 2011) and approved by the Lifespan Animal Welfare Committee at Rhode Island Hospital. Hearts were excised, retrogradely perfused through the aorta with (in mmol/l) 130 NaCl, 24 $NaHCO_3$, 1.0 $MgCl_2$, 4.0 KCl, 1.2 NaH_2PO_4, 5 dextrose, 25 mannitol, and 1.25 $CaCl_2$, at pH 7.4, gassed with 95% O_2 and 5% CO_2, and stained with the voltage-sensitive dye di-4-ANEPPS (Invitrogen). Hearts were placed in a water-heated chamber to maintain temperature at 37.0 ± 0.2°C, and 5 μmol/l blebbistatin were added to reduce movement artifact. Perfusion rate was set to 20 ml/min. Twelve LQT2 rabbits were used in this project. The atrioventricular (AV) node was ablated to control heart rate using a cautery unit (World Precision Instruments). After ablation, the rabbits exhibited a slower heart rate, with the cycle length typically ranging from 700 to 2,000 ms. If the cycle length was longer than 2,000 ms, the base of the right ventricle (RV) was paced at a cycle length of 2,000 ms. Isoproterenol was delivered as a bolus injection via the bubble trap (5 ml, 140 nM) to hearts to trigger ectopic excitations and polymorphic ventricular tachycardia (pVT). Fluorescence images of APs were recorded from the anterior surface of the heart using a CMOS camera (100 × 100 pixels, 1,000 frames/s, 2.0 × 2.0 cm^2 field of view, Ultima-L; SciMedia). Activation maps and APD maps were generated using dF/dt and dF^2/dt^2 using digital image analysis routines as previously described (24).

Computer Simulation

Tissue models. Computer simulations were carried out in single cell model, one-dimensional (1D) and two-dimensional (2D) isotropic monodomain tissue models. The governing partial differential equation for voltage is

$$\frac{\partial V}{\partial t} = -\left(I_{ion} + I_{sti}\right)/C_m + D\nabla^2 V \quad (1)$$

where C_m is the membrane capacitance, which was set as $C_m = 1$ μF/cm^2, and D is the diffusion coefficient, which was set as $D = 0.0005$ cm^2/ms. This resulted in a conduction velocity of 0.036 cm/ms in the 1D cable. I_{ion} is the total ionic current density described by the rabbit ventricular AP model by Mahajan et al. (31) with a modified $I_{Ca,L}$ detailed below. I_{sti} is the stimulus current density of amplitude 50 μA/cm^2 and duration 2 ms.

Ionic current and AP models. In the rabbit ventricular AP model by Mahajan et al. (31), $I_{Ca,L}$ was formulated using Markov transitions. Although it can exhibit phase 2 EADs (52, 53), it involves a number of parameter changes, and the EAD amplitude is relatively small. Moreover, it is inconvenient to change the window $I_{Ca,L}$ alone without changing other properties due to the Markov scheme. To promote EADs and change the window $I_{Ca,L}$, we substituted the Markov formulation of $I_{Ca,L}$ by a Hodgkin-Huxley formulation by Luo and Rudy (28) and Zeng et al. (70). The $I_{Ca,L}$ formulation in the original Mahajan et al. model (31) is

$$I_{Ca,L} = G_{Ca,L}\, P_o i_{Ca,L} \quad (2)$$

where $G_{Ca,L}$ is the maximum conductance of $I_{Ca,L}$, P_o is the open probability of the channel, and $i_{Ca,L}$ is the unitary current of the channel. We substituted P_o by

$$P_o = d \cdot f \cdot f_{Ca} \quad (3)$$

where d is the voltage-gated activation gating variable and f is the voltage-dependent inactivation gating variable taken from the Luo and Rudy model (28), and f_{Ca} is the Ca-dependent inactivation gating variable taken from Zeng et al. (70). We substituted the intracellular Ca concentration with submembrane Ca concentration (c_s) in the f_{Ca} formulation, i.e.,

$$f_{Ca} = \frac{1}{1 + \frac{c_s}{0.6}} \quad (4)$$

Figure 1*A* shows the current-voltage (*I–V*) curves of peak $I_{Ca,L}$ for different $G_{Ca,L}$.

A wide range of peak $I_{Ca,L}$ has been reported in normal rabbit ventricular myocytes (6, 26, 31, 38, 57), ranging from 5 to 18 pA/pF. According to Fig. 1*A*, this range roughly corresponds to $G_{Ca,L}$ 30–150 mmol/(cm,C) in our model. We chose $G_{Ca,L} = 40$ mmol/(cm,C) for our normal control model, which gives rise to a peak $I_{Ca,L}$ ~6 pA/pF during an AP. The maximum conductance of the slow component of the delayed-rectifier potassium current (G_{Ks}) was set as $G_{Ks} = 0.5$ mS/cm^2 for control, which gives rise to a peak slow component delayed-rectifier potassium current (I_{Ks}) of 0.4 pA/pF during an AP, roughly the same as the measurements in rabbit experiments (6, 26, 38). We also set the Na/Ca exchange pump strength as $g_{NaCa} = 1.0$ μM/s and clamped intracellular Na concentration = 8 mM. Other parameters were the same as in the original Mahajan et al. model. This gives rise to an APD around 210 ms for the normal control (Fig. 1*B*).

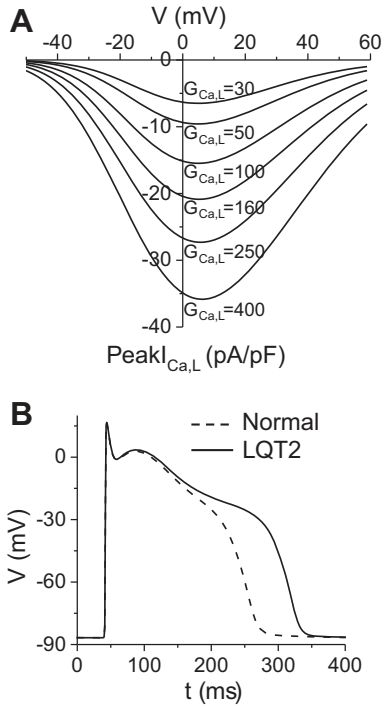

Fig. 1. L-type calcium current ($I_{Ca,L}$) and action potentials (APs) of the modified rabbit ventricular cell model. *A*: peak $I_{Ca,L}$ vs. holding voltage under voltage clamp for different maximum conductance values of $I_{Ca,L}$ [$G_{Ca,L}$, mmol/(cm,C)]. Note that a 5-fold increase in $G_{Ca,L}$ (from 50 to 250) resulted in roughly a 3-fold increase in peak $I_{Ca,L}$. *B*: AP under normal control condition (dashed), $G_{Ca,L}$ = 40 mmol/(cm,C), and AP under LQT2 condition (solid), in which we set G_{Kr} = 0 from the normal control condition. Pacing cycle length was 1 s.

We completely blocked the rapid component of the delayed-rectifier potassium current [I_{Kr}, by setting the maximum conductance of I_{Kr} to 0, i.e., maximum conductance of the rapid component of the delayed-rectifier potassium current (G_{Kr}) = 0] from the normal control to simulate LQT2 since I_{Kr} was almost undetectable in the transgenic LQT2 rabbit hearts (6). This resulted in an APD around 280 ms for LQT2 control (Fig. 1*C*). These APD values agree with experimental measurements in normal and transgenic LQT2 rabbit hearts (6).

Modeling the Effects of Isoproterenol

We simulated the effects of isoproterenol by increasing the conductance of $I_{Ca,L}$ and I_{Ks}. As shown by Liu et al. (26), the time courses of activation of the two currents caused by isoproterenol are different, with $I_{Ca,L}$ being activated earlier. Therefore, infusion of isoproterenol first increases APD and APD dispersion and then decreases APD and APD dispersion, which was demonstrated in previous experimental studies (26, 56). For simplicity, we used different combinations of $I_{Ca,L}$ and I_{Ks} to model the isoproterenol effects. Based on Liu et al. (26), isoproterenol can double $I_{Ca,L}$ and triple I_{Ks} in rabbit ventricular myocytes, and thus the maximum peak $I_{Ca,L}$ can reach 30–40 pA/pF after isoproterenol. This corresponds to a $G_{Ca,L}$ >300 mmol/(cm,C) in our model. Therefore, in this study, we explored the $G_{Ca,L}$ range 30–400 mmol/(cm,C) in our simulations.

Modeling Repolarization Heterogeneities in Tissue

In the real hearts, repolarization heterogeneity or gradient is a result of heterogeneous distributions of the ionic current as well as Ca cycling properties. For the sake of simplicity, in most of the tissue simulations, we used heterogeneous I_{Ks} conductance to simulate APD dispersion or RG while keeping other currents uniform except for the population-based simulations. Twofold regional difference of I_{Ks} in rabbit hearts was reported (25). Data from other species also showed a 1.5- to 2-fold regional difference (18, 36). In the 2D tissue model, we used G_{Ks} = 0.43 mS/cm^2 in the long APD region and 0.7 mS/cm^2 in the short APD region for normal control, which is within the twofold range. However, to generate larger APD gradients and systematically investigate the mechanisms of PVCs, we explored a range of regional difference of I_{Ks} conductance much larger than the twofold differences in our simulations of the 1D cable model.

Population-Based Simulations

To systematically investigate the diversity of heterogeneities in the real hearts, we carried out a large number of 1D cable simulations to cover a wide range of heterogeneities. In these simulations, APD heterogeneities were simulated using heterogeneous $I_{Ca,L}$, I_{Ks}, and transient outward K current (I_{to}) distributions, and parameter combinations were selected to simulate different APD gradients. The detailed settings for these simulations are presented in RESULTS.

Simulation Methods

An explicit Euler method and the Rush-Larsen method (48) were used to integrate the differential equations with a fixed time step Δt = 0.01 ms. For the simulations of 1D and 2D tissue, a space step Δx = Δy = 0.015 cm was used. I_{sti} was delivered to the first five cells from one end of the 1D cable or from the left side of the 2D tissue with a duration of 2 ms and magnitude of 50 μA/μF. The 1D cable length was 200 cells (corresponding to 3 cm) unless otherwise specified. The 2D tissue size was 300 × 300 cells (corresponding to 4.5 × 4.5 cm^2). The heterogeneous region in 2D tissue was a circular area in the center with a radius r = 0.9 cm. No-flux boundary conditions were used. Except for the simulations of pause-induced PVCs, for all other simulations, a single pacing simulation was applied after the cells reached their steady-state resting states. Simulations were carried out using Graphic Processor Units (Nvidia Tesla K20) and C programing language.

RESULTS

RG Induced PVCs and Arrhythmias in Transgenic LQT2 Rabbit Hearts

Our previous study (6) has shown that, under the normal condition, 60% of the transgenic LQT2 rabbits die suddenly at the age of one year. ECG monitoring from these rabbits showed pause-induced pVTs, agreeing with the well-known clinical observation that pVTs or TdPs are pause dependent in LQT2 patients (14, 44, 54, 63). Ideally, one should capture the pVT events under normal conditions to investigate the mechanisms underlying spontaneous initiation of ventricular arrhythmias. However, it is almost impossible to capture these episodes using optical mapping experiments under normal conditions since the arrhythmia events are very rare. To increase the arrhythmia events so that one can optically map the incidence of spontaneous initiation of ventricular arrhythmias, we used AV ablation to slow the heart rate. After the AV node was ablated in these rabbits, the heart rates were slowed, exhibiting cycle lengths typically longer than 700 ms. To avoid the heart rate to be too slow, a pacing stimulus was delivered to the base of RV to excite the heart if the cycle length was longer than 2,000 ms. Because the heart was paced either by spontaneous firings from the Purkinje fiber or by external stimuli from the RV base, we call these beats non-PVC beats or excitations to distinguish them from the PVC beats.

We mapped 12 LQT2 rabbit hearts from the anterior with a field view of 2 × 2 cm^2, which partially covers both the RV and the left ventricle (LV), as indicated in Fig. 2*A*. After isoproterenol infusion, PVCs and arrhythmias occurred in these hearts. Figure 2*B* shows an example of APD distribution (*left*) and a space-time plot of APs (*right*) under isoproterenol for a non-PVC beat in a LQT2 rabbit heart. A phase 2 EAD (arrow) occurred in the long APD region. Ten seconds later in the same heart, an ectopic beat occurred (Fig. 2*C*). A phase 2 EAD (arrow) was still seen in the long APD region, and a focal excitation (*) originated from the APD gradient region propagated around the long APD region, forming a short-lived reentry [Supplemental Movie S1 (Supplemental material for this article is available on the Journal website.)]. Figure 2*D* shows another scenario of a focal excitation originating from the APD gradient region and propagating around the long APD region, as indicated by the APD map of a normal beat and the activation map of the PVC. Figure 2*E* shows a case in which the repetitive focal excitations propagated in all directions without local block. These ectopic events either manifested as single or multiple PVCs or eventually led to polymorphic ventricular arrhythmias in the LQT2 rabbit hearts.

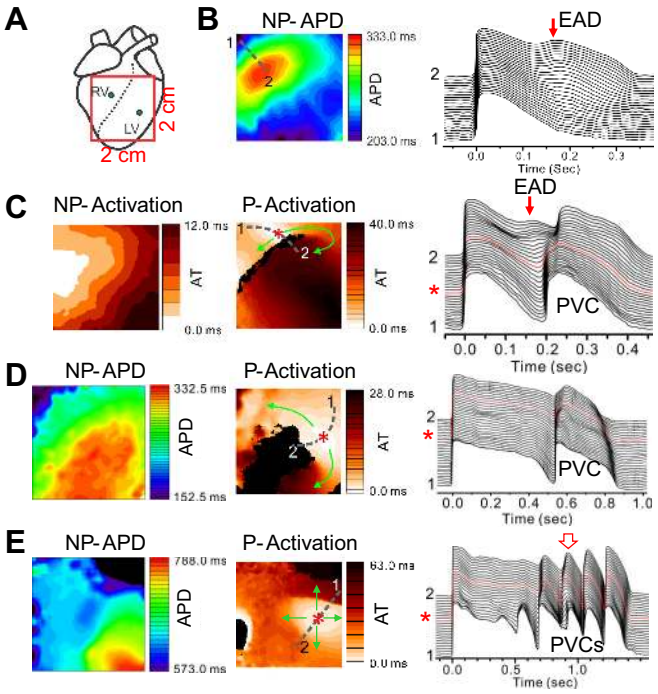

Fig. 2. Repolarization gradient-induced premature ventricular complexes (PVCs) in transgenic LQT2 rabbit hearts. *A*: schematic plot of the optical mapping field on the anterior surface. *B*: action potential duration (APD) distribution (*left*) and space-time plot of voltage (*right*, along the broken line from position 1 to position 2 marked on *left*) for a non-PVC beat after infusion of isoproterenol. *C*: 10 s later in the same heart as in *B*, a PVC was triggered following a non-PVC excitation (see *right*). *Left*, activation map of the normal excitation. *Middle*, activation map of the focal excitation. Arrows indicate the directions of propagations, and * marks the initiation site. *Right*, space-time plot of voltage showing the non-PVC and the focal excitation (marked as PVC) beats. *D*: a PVC following a non-PVC excitation in a different rabbit heart. *Left*, APD map of a non-PVC excitation beat. *Middle*, activation map of the PVC beat. *Right*, space-time plot of voltage showing the non-PVC and the focal excitation (marked as PVC) beats. *E*: repetitive PVCs originating from the same site propagate in all directions in a different rabbit heart. *Left*, APD map of a non-PVC excitation beat. *Middle*, activation maps of the second PVC beat as marked by the open arrow on the *right*. *Right*, space-time plot of voltage showing the non-PVC and the PVC beats. The abbreviated labels above the maps are: NP-APD-APD map of a non-PVC beat; NP-Activation-Activation map of a non-PVC beat; and P-Activation-Activation map of a PVC beat.

In 12 rabbit hearts, we examined 127 pVT events, 42 of which (33.0%) had PVCs that can be categorized into the type shown in Fig. 2, *C* and *D*, i.e., PVCs originated from the RG region and propagated toward the short APD region only, forming a short-lived reentry, whereas 10 pVT events (7.9%) had PVCs that can be categorized into the type shown in Fig. 2*E*, where PVCs propagated in all directions. The remaining 75 pVT events cannot be categorized because the initiation sites of PVCs were outside the mapping field.

RG induced PVCs and Reentry in a 2D LQT2 Rabbit Tissue Model

To recapitulate the experimental observations, we carried out simulations of 2D heterogeneous tissue. For simplicity, we created a circular region in the center of the tissue and paced from the left edge. Heterogeneity was simulated by a lower I_{Ks} in the circular area to prolong APD. Figure 3*A* shows the APD distribution for normal control, in which APD varied from 185 to 210 ms. After removing I_{Kr} to simulate LQT2, APD varied from 215 to 275 ms (Fig. 3*B*). These data correspond to our published experimental measurements of APD and dispersion in control and transgenic LQT2 rabbit hearts (6, 72). We then increased $I_{Ca,L}$ and I_{Ks} to simulate the effects of isoproterenol (26). At a low isoproterenol level, APD was prolonged, and dispersion was increased, with an EAD occurring in the long APD region (Fig. 3*C*), similar to the experimental data shown in Fig. 2*B*. As the isoproterenol effect was enhanced (Fig. 3*D* and Supplemental Movie S2), APD increased further, and a focal excitation originated from the RG region at the right side of the long APD region and propagated around the long APD region. The two wavefronts collided in the other side of the long APD region without forming a reentrant circuit, resulting in an ectopic beat. This scenario is the same as that shown in the LQT2 hearts in Fig. 2, *C* and *D*. Whether a true reentry can form depends on the size of the long APD region, and, when we increased the size of that region, reentry formed (Supplemental Movie S3). On the other hand, when we lengthened the APD further in the long APD region, multiple ectopic beats occurred (e.g., Supplemental Movie 4). In our computer model, the heterogeneity was symmetrical, but, due to the conduction delay, the focal excitation occurred in one side of the long APD region. For asymmetric or irregular heterogeneities as in real tissue, the location of the focal site will depend on the specific structure of the heterogeneity and the conduction direction. In this simplified tissue model, when we paced the whole tissue simultaneously, the spontaneous excitations occurred in all sides, resulting in target patterns (Fig. 3*E* and Supplemental Movie S5) similar to the experimental patterns shown in Fig. 2*E*.

Mechanisms of RG-Induced Unidirectionally Propagating PVCs

To investigate the underlying mechanisms and the roles of EADs and RG in the spontaneous genesis of PVCs, we carried out simulations using 1D heterogeneous cable models, system-

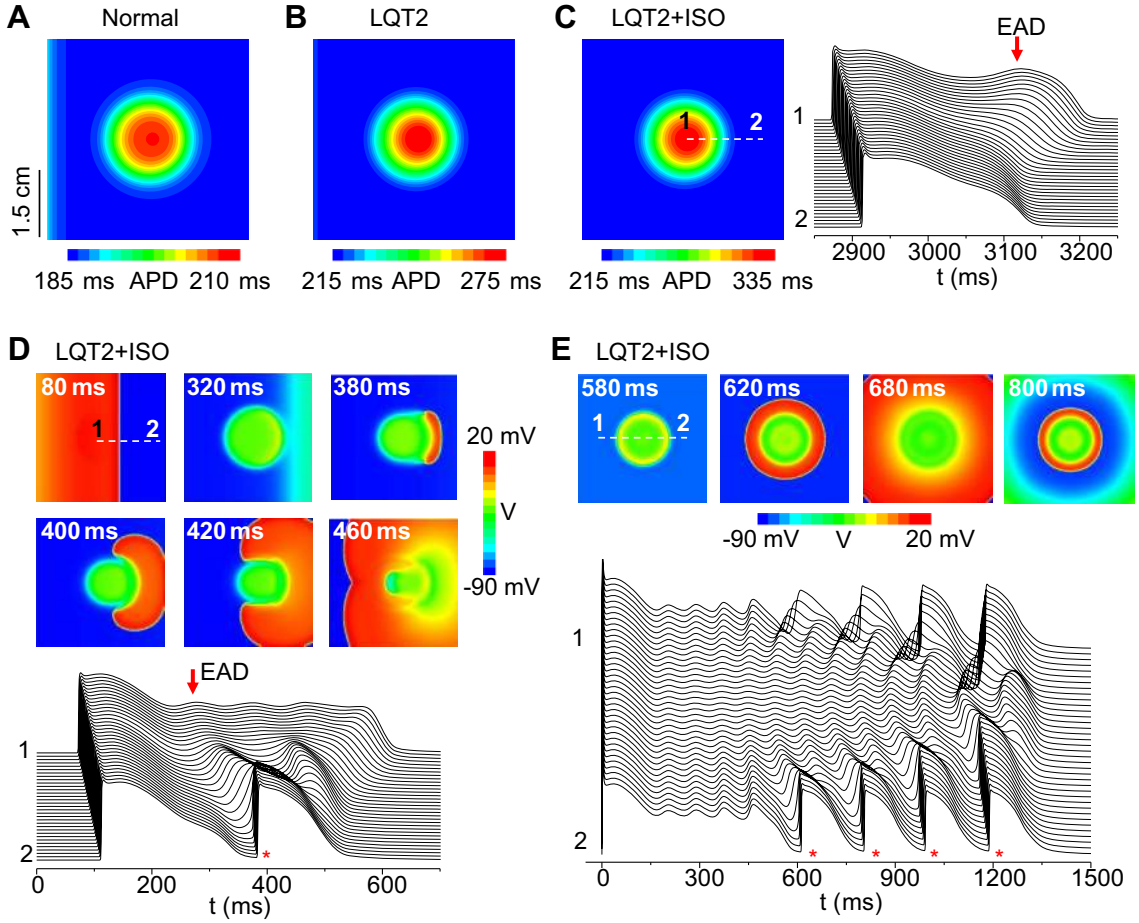

Fig. 3. Repolarization gradient-induced PVCs in a 2D tissue model. *A*: APD distribution under normal control. $G_{Ca,L}$ = 40 mmol/(cm,C), maximum conductance of the slow component of the delayed-rectifier potassium current (G_{Ks1}) = 0.7 mS/μF; G_{Ks2} = 0.43 mS/μF; and G_{Kr} = 0.01 mS/μF. *B*: APD distribution under simulated LQT2 (G_{Kr} = 0). The parameters are the same as in *A* except G_{Kr} = 0. *C*: APD distribution (*left*) and space-time plot of voltage (*right*) under simulated LQT2 conditions with a low isoproterenol effect. $G_{Ca,L}$ = 60 mmol/(cm,C), G_{Ks1} = 0.9 mS/μF, and G_{Ks2} = 0.56 mS/μF. Note the difference in color scales in *A*–*C*. *D*: voltage snapshots (marked by timing) and space-time plot (*bottom*) under simulated LQT2 with a higher isoproterenol effect. $G_{Ca,L}$ = 176 mmol/(cm,C), G_{Ks1} = 1.1 mS/μF, and G_{Ks2} = 0.7 mS/μF. *E*: voltage snapshots (marked by timing) and space-time plot (*bottom*) under simulated LQT2 with a high $I_{Ca,L}$. $G_{Ca,L}$ = 276 mmol/(cm,C), G_{Ks1} = 0.7 mS/μF, and G_{Ks2} = 0.6 mS/μF. The white broken lines in *C*, *D*, and *E* mark the locations (from 1 to 2) for the corresponding space-time plots of voltage. Red arrows in *C* and *D* mark early afterdepolarizations (EADs). * in *D* and *E* marks the PVC beats. Tissue size is 4.5 cm × 4.5 cm. APD gradient was modeled by a smaller G_{Ks} (G_{Ks2}) in the circular region (r = 0.9 cm) in the center, and all other parameters in the tissue are uniform. A stimulus was given at the left side of the tissue in all cases except *E* in which the stimulus was given to all cells at time (t) = 0.

atically exploring the parameters detailed in the sections below.

Cellular phase 2 EADs, RG-induced tissue-scale phase 3 EADs, and PVCs. To investigate the roles of cellular phase 2 EADs in PVC formation in tissue, we first carried out simulations of an uncoupled single cell to explore the AP behaviors under the condition of simulated LQT2 (G_{Kr} = 0) for different $G_{Ca,L}$ and G_{Ks}. We scanned $G_{Ca,L}$ from 40 to 400 mmol/(cm,C) and G_{Ks} from 0.01 to 1 mS/cm^2. Figure 4*A* shows the observed AP behaviors: *1*) normal repolarization, occurring at large G_{Ks} and small $G_{Ca,L}$; *2*) repolarization failure, occurring at small G_{Ks} and large $G_{Ca,L}$; and *3*) EADs. In the EAD zone, we plotted the EAD amplitude (defined in the *inset* of Fig. 4*A*) in color scales. We recorded the largest EAD in an AP. The maximum EAD amplitude in the scanned parameter ranges was ~40 mV. The EAD amplitude tended to be larger for a larger $I_{Ca,L}$ in general. However, note that the EAD amplitude color map is discretized, and large-amplitude EADs could occur for small $I_{Ca,L}$. All EADs were phase 2 EADs with takeoff potentials above −40 mV (data not shown); −40 mV is close to the $I_{Ca,L}$ activation threshold, indicating that these EADs were the result of reactivation of $I_{Ca,L}$.

We then carried out simulations in a heterogeneous 1D cable for PVC formation. The 1D cable was composed of two types of cells distinguished by different G_{Ks} (G_{Ks1} and G_{Ks2} as shown in the *inset* of Fig. 4*B*). We fixed G_{Ks1} = 1 mS/cm^2 and varied G_{Ks2} to alter RG. The cable length was 200 cells, and the length of the G_{Ks2} (long APD) region was 50 cells. A single stimulus was applied from the short APD side to induce AP conduction. We scanned G_{Ks2} from 0.01 to 1 mS/cm^2 and $G_{Ca,L}$ of the whole cable from 40 to 400 mmol/(cm,C); therefore, the G_{Ks} and $G_{Ca,L}$ ranges in the long APD region were the same as those for the single cell in Fig. 4*A*. Figure 4*B* shows the parameters that exhibit PVCs (olive) and no PVCs (white). Compared with the occurrence of EADs in the uncoupled single cell (Fig. 4*A*), the occurrence of PVCs in the heterogeneous 1D cable (Fig. 4*B*) required a two- to threefold increase in $I_{Ca,L}$ (see Fig. 1*A* for the relationship between peak $I_{Ca,L}$ and

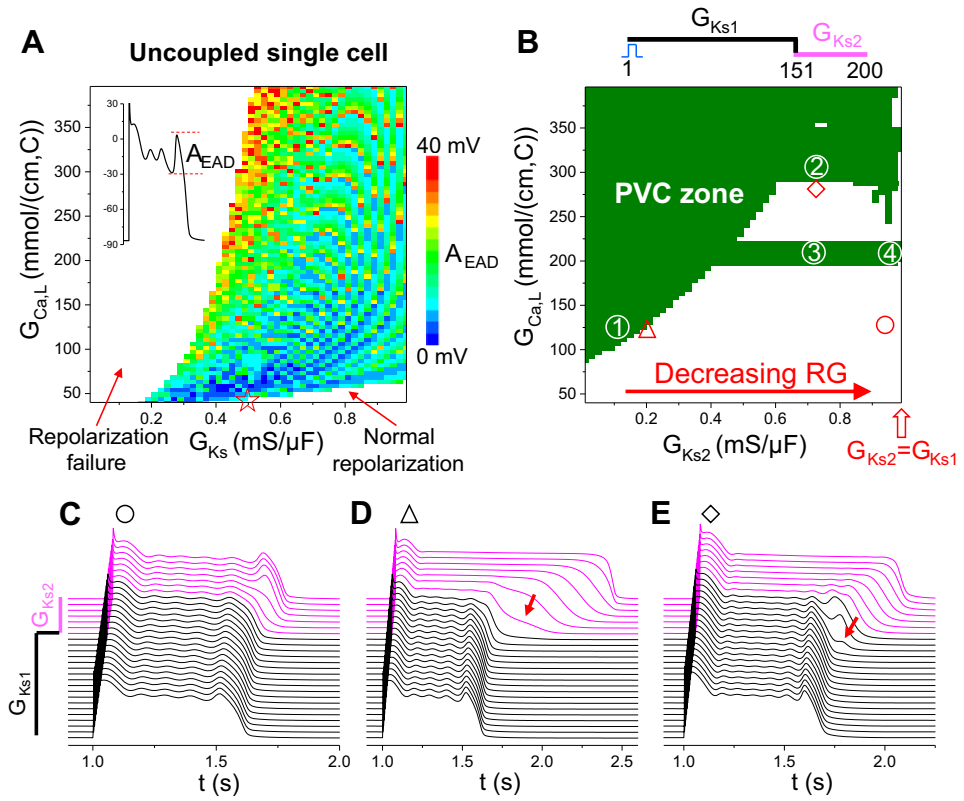

Fig. 4. Tissue-scale EADs and PVCs in a heterogeneous 1D cable. *A*: EAD amplitude (A_{EAD}) distribution from an isolated single cell by scanning $G_{Ca,L}$ and G_{Ks}. G_{Kr} = 0. A_{EAD} (indicated by color) was defined as in the *inset*, which was the largest of the EADs in an AP. The red star on the *x*-axis indicates the control condition of LQT2 whose AP was shown in Fig. 1*C*. *B*: PVC zones (olive) for different combinations of $G_{Ca,L}$ of the whole cable and G_{Ks} (G_{Ks2}) in the long APD region. Simulations were carried out in a 200-cell cable with G_{Ks1} being used for the first 150 cells and G_{Ks2} for the remaining 50 cells. All other currents are uniform in the whole cable. G_{Ks1} = 1 mS/μF and G_{Kr} = 0. *C*–*E*: space-time plots of voltage for three different combinations of $G_{Ca,L}$ and G_{Ks2} as marked by symbols in *B*. $G_{Ca,L}$ = 125 mmol/(cm,C) and G_{Ks2} = 0.942 mS/μF for *C*, $G_{Ca,L}$ = 120 mmol/(cm,C) and G_{Ks2} = 0.19 mS/μF for *D*, and $G_{Ca,L}$ = 287 mmol/(cm,C) and G_{Ks2} = 0.71 mS/μF for *E*. Arrows in *D* and *E* indicate phase 3 EADs. The magenta traces in *C*–*E* are voltage traces from the cells with the small G_{Ks} (G_{Ks2}), and the black ones are from the cells with the large G_{Ks} (G_{Ks1}).

$G_{Ca,L}$). Note that, in the uncoupled single cell, repolarization failure occurred when G_{Ks} was relatively small, but, when the cells were coupled in the 1D heterogeneous cable, they repolarized with long APDs (such as the examples shown in Figs. 4*D* and 6*A*).

In the no-PVC zones, the cellular phase 2 EADs were either suppressed or confined to the long APD region (see Fig. 4*C*). At the border near the PVC zone, tissue-scale EADs were generated when RG was large (Fig. 4*D*) and/or $I_{Ca,L}$ was large (Fig. 4*E*). When RG was large, the phase 3 repolarization was markedly slowed in the RG region (arrow in Fig. 4*D*). These slow phase 3 repolarizations were previously called phase 3 EADs (16) and were very similar to those observed in experiments by Maruyama et al. (32). A further increase in RG (from "△" to "1" in Fig. 4*B*) resulted in PVCs. When $I_{Ca,L}$ was large, small depolarizations could occur in phase 3 of the APs in the cells in the RG region (arrow in Fig. 4*E*). Because no EADs were present in the long APD region, and the takeoff potential of EADs in uncoupled single cells was above −40 mV, these are tissue-scale EADs caused by the RG, not a single cell property. If $I_{Ca,L}$ was increased further (from "◇" to "2" in Fig. 4*B*), these EADs then grew toward the short APD region and successfully propagated into PVCs.

Note that the APD in the long APD region in Fig. 4*D* is very long (>1 s), which is much longer than that under the normal condition. However, it is not uncommon to see very long APDs in rabbit hearts under experimental conditions with slow pacing. For example, in the optical mapping by Maruyama et al. (32) and the microelectrode recordings by Yan et al. (67) in drug-induced LQT2 rabbits, very long APDs were demonstrated at slow heart rates.

By comparing Fig. 4, *A* and *B*, one can see that a large parameter region that gave rise to EADs in uncoupled single cell did not exhibit PVCs in the 1D cable although large-amplitude cellular phase 2 EADs occurred in this parameter region. To systematically investigate the effects of RG on cellular phase 2 EADs, we performed additional simulations in a 1D cable by altering RG, the size of the EAD region, and gap junction coupling (Fig. 5). We first simulated a homogeneous cable in which a cellular EAD occurred in every cell with an amplitude of ~35 mV (Fig. 5*A*). We then gradually increased G_{Ks} (G_{Ks1}) in the two ends of the cable (see *inset* in Fig. 5*B*) to investigate the EAD behaviors. Figure 5*B* shows an example in which the EAD still occurred in the center region but was suppressed in the border regions, and thus the EAD cannot propagate out the center region to generate a PVC in the short APD regions. We systematically scanned the size of the center region (L) and the G_{Ks1} value for the control diffusion constant (D = 0.0005 cm^2/ms) and measured the corresponding EAD amplitude in the center of the cable (Fig. 5*C*, *left*) and in one of the border regions (Fig. 5*C*, *right*). When L was short, the EAD was completely suppressed unless the cable was almost homogeneous (G_{Ks1}~G_{Ks2}). When L was large, the EAD was suppressed in the RG regions but remained intact in the center region (compare Fig. 5*C*, *left* and *right*). Therefore, as RG was increased, the EAD was confined to the long APD region, which could not transmit to the RG region to induce a PVC. Similarly, we scanned D and G_{Ks1} for a fixed center region (L = 120 cells) and measured the corresponding EAD amplitude in the center of the cable (Fig. 5*D*, *left*) and in one of the border regions (Fig. 5*D*, *right*). The EAD was completely suppressed when both D and G_{Ks1} are large (Fig. 5*D*, *left*). No

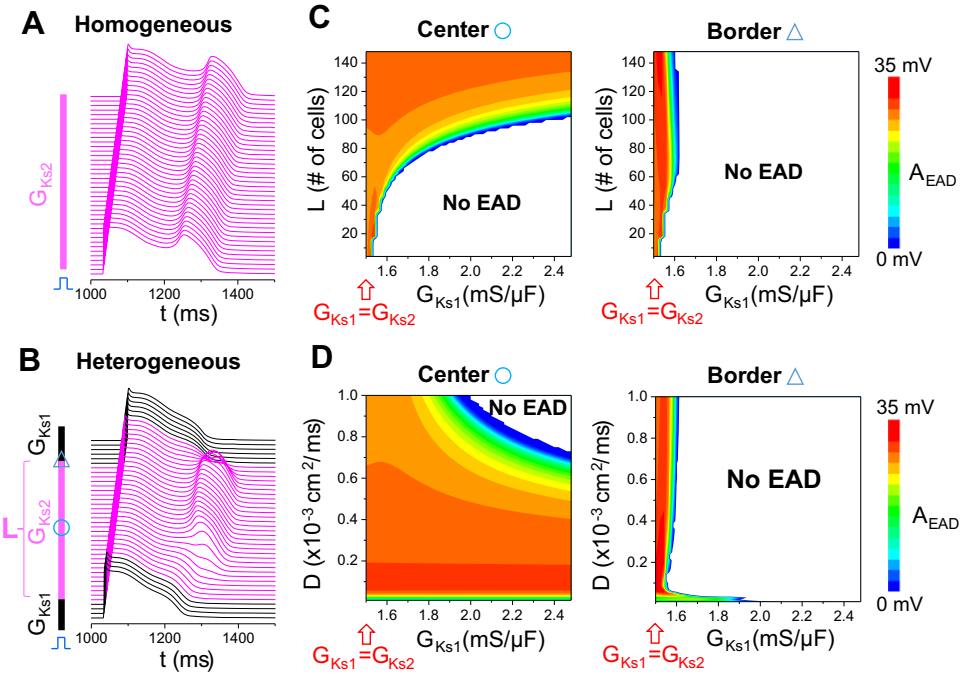

Fig. 5. Suppression of cellular phase 2 EADs by repolarization gradient (RG) in a 1D cable. *A*: space-time plot of voltage from a homogeneous cable showing a cellular EAD in every cell. $G_{Ca,L}$ = 120 mmol/(cm,C), G_{Kr} = 0, and G_{Ks1} = G_{Ks2} = 1.5 mS/μF. A large cellular EAD (~35 mV in magnitude) occurs in the AP. *B*: same as *A*, but the cable is heterogeneous. The *inset* shows the distribution of the slow component of the delayed-rectifier potassium current (I_{Ks}). The cable length is 320 cells, the middle 120 cells (magenta) of which exhibit EADs when uncoupled (G_{Ks2} = 1.5 mS/μF as in the homogeneous cable in *A*), and the cells on both sides have a shorter APD (G_{Ks1} = 1.7 mS/μF). For visualization purpose, not all G_{Ks1} cells in the cable are plotted in this panel. *C*: *left*, EAD A_{EAD} (defined as in Fig. 4*A* and plotted in color scale as indicated by the color bar) from a cell in the middle of the cable vs. G_{Ks1} and length of the middle segment (*L*, defined in *B*). *Right*, A_{EAD} from a cell in the gradient region marked by the triangle in *B* vs. G_{Ks1} and *L*. Diffusion constant *D* = 0.0005 cm^2/ms. *D*: *left*, A_{EAD} from a cell in the middle of the cable vs. G_{Ks1} and diffusion constant *D*. *L* = 120. *Right*, A_{EAD} from a cell in the gradient region marked by the circle in *B* vs. G_{Ks1} and diffusion constant *D*.

EAD could be detected in the RG region, even after *D* is reduced by several fold (Fig. 5*D*, *right*).

Our simulation results in Figs. 4 and 5 suggest that PVCs may not be a direct consequence of phase 2 EAD propagation since cellular phase 2 EADs tend to be suppressed or confined by RG. However, we note that, whether a cellular phase 2 EAD can propagate into a PVC or not, or under what condition it can propagate into a PVC, cannot be concluded merely by simulations of a specific model. More rigorous theoretical or systematic analyses are still needed. On the other hand, our simulations demonstrated that new mechanisms occurred at the tissue scale to generate PVCs, which are tissue-scale dynamical instabilities and are different from the traditional thinking of PVC as a consequence of phase 2 EAD propagation. We identified two different mechanisms of PVC genesis in the 1D cable, as described in detail in the following sections.

Large RG-induced PVCs. In this mechanism, PVCs occur when the RG is larger than a critical value and strongly depends on the properties of the cells in the long APD region. Figure 6*A* shows a PVC (*) caused by this mechanism (from *location 1* in Fig. 4*B*). Figure 6*B* is the corresponding space-time plot of $dV/dt > 0$ showing that the leading site of depolarization initiating the PVC occurred in the RG region. To demonstrate that a critical APD gradient is needed, rather than a sudden change from G_{Ks1} to G_{Ks2}, we changed G_{Ks1} to G_{Ks2} linearly cross a region (as in the *inset* of Fig. 6*C*) to reduce the APD gradient. When this linear region exceeded the length that reduces the maximum APD gradient below a critical value, PVCs no longer occurred (Fig. 6*C*). Note that the APD in the long APD region became slightly longer, and the APD in the short APD region remained unchanged (compare Fig. 6, *C* and *A*), but the APD gradient was reduced in the RG region due to the gradual transition from G_{Ks1} to G_{Ks2}. This indicates that a critical RG is needed for PVCs to occur. Using this gradual G_{Ks1}-to-G_{Ks2} transition, we obtained the APD gradient thresholds for a couple of $G_{Ca,L}$ and G_{Ks2} combinations along the left border between the PVC and no-PVC zones in Fig. 4*B*, which were plotted in Fig. 6*D* in a bar graph. The APD gradient threshold decreased as $I_{Ca,L}$ conductance increased. However, we found that a large APD gradient per se was not sufficient for causing PVCs; other conditions were required. To show this, we clamped the cells in the long APD region at their plateau voltages, which greatly increased the voltage or APD gradient, but surprisingly PVCs no longer occurred (Fig. 6*E*). This indicates that, in addition to a large APD gradient, the cells in the long APD region have to be free of oscillation for PVC formation. This also demonstrates that the PVC is not simply "prolonged repolarization-dependent reexcitation" proposed previously (5). As shown in Figs. 4*D* and 6*B*, before the transition to PVCs, the cells in the short APD region pulled down the voltage of the cells in the long APD region, which resulted in a very slow phase 3 repolarization [or phase 3 EADs (16)] of the cells in the long APD region. As the RG increased further, spontaneous depolarizations suddenly occurred in the long APD side of the RG region to result in PVCs. No cellular EADs were involved in the PVC

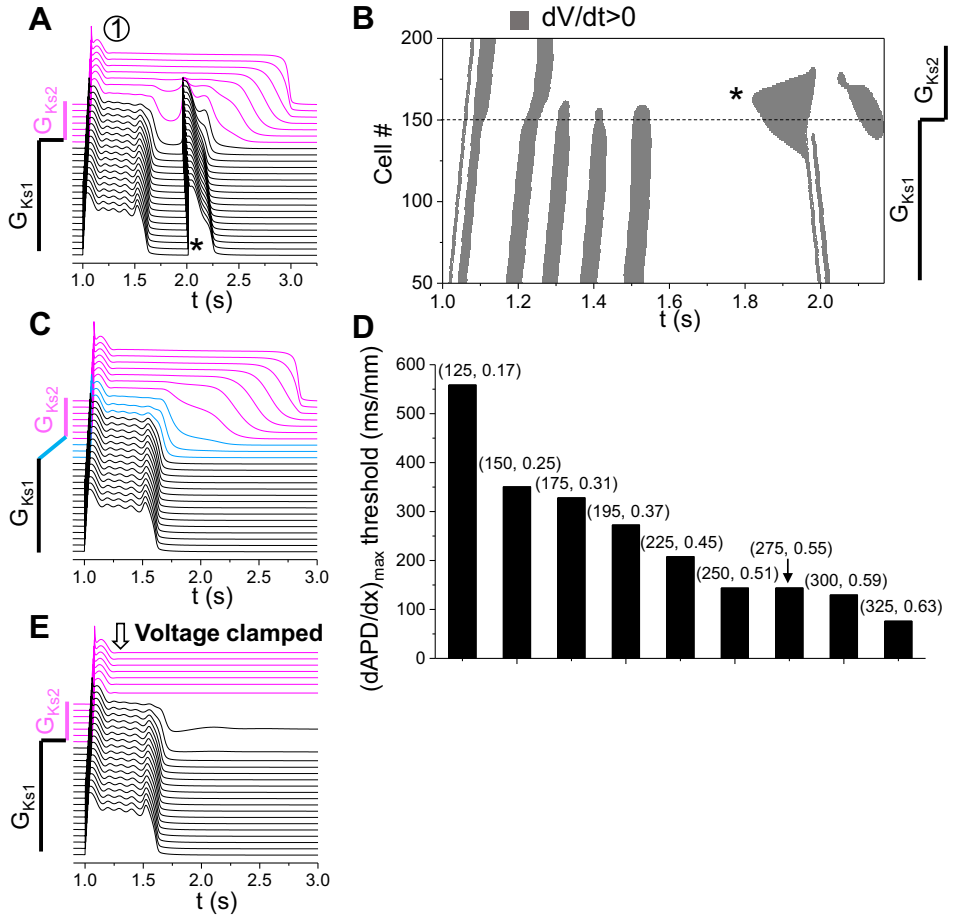

Fig. 6. Large RG-induced PVCs. *A*: space-time plot of voltage showing a PVC (*) generated due to RG via the first mechanism (location "1" in Fig. 4*B*). $G_{Ca,L}$ = 120 mmol/(cm,C) and G_{Ks2} = 0.15 mS/μF. *B*: space-time plot of $dV/dt > 0$ for the voltage shown in *A*. *C*: same as *A*, but the change of G_{Ks1} to G_{Ks2} occurred across 20 cells, and the PVC disappeared. *D*: critical APD gradient (maximum APD gradient in the cable) for PVC genesis for the parameter set ($G_{Ca,L}$, G_{Ks2}) as marked. *E*: same as *A*, but the cells in the long APD region are voltage clamped at their value at t = 1,160 ms.

genesis, and thus the PVCs were not originated from propagation of EADs. The occurrence of PVCs was caused by a tissue-scale dynamical instability that depends on not only the properties of tissue heterogeneities but also the cellular properties.

Small RG or boundary effect-induced PVCs. This mechanism of PVC formation does not require a critical RG but strongly depends on the properties of the cells in the short APD region. Figure 7*A* shows a PVC (*) of this mechanism (from *location 2* in Fig. 4*B*). Figure 7*B* is the corresponding space-time plot of $dV/dt > 0$ showing that the leading site of depolarization initiating the PVC occurred in the RG region. Following the same method to reduce APD gradient by changing G_{Ks1} to G_{Ks2} gradually as in Fig. 6*C*, we could not eliminate the PVC but created more PVCs (Fig. 7*C*). This indicates that a critical RG is unnecessary, which is opposite to the mechanism of large RG-induced PVCs. When we clamped the voltages of the cells in the long APD region the same way as we did in Fig. 6*E*, the oscillations became sustained (Fig. 7*D*). This indicates that the oscillations were generated in the short APD side in the RG region. Therefore, in this mechanism, cells in the long APD region provide an electrical source to cells in the short APD region to cause tissue-scale phase 3 EADs in the RG region. When $I_{Ca,L}$ is strong enough, these EADs can then grow in the short APD region to result in PVCs. This mechanism requires that the cells in the short APD region are prone to cellular EADs or oscillations in the repolarizing phase. Note that, in this mechanism, a PVC is also not a result of EAD propagation but a tissue-scale dynamical instability dependent on both cellular properties and RG.

We observed two special cases of this mechanism: a PVC occurred at the tissue boundary (Fig. 7*E*) or started from the RG region when the RG was very small (Fig. 7*F*). In both cases, a cellular EAD was present in the long APD region, which provided an additional electrical source for PVC formation. However, only when the RG was very small could an EAD survive at the RG region (see Fig. 5) and become the source of a PVC. At the tissue boundary, the no-flux boundary condition caused a slightly shorter APD at the boundary region, resulting in a small RG to facilitate this mechanism. Because it was a boundary effect, region 3 in Fig. 4*B* was a horizontal bar that did not depend on the RG caused by the G_{Ks} heterogeneity in our model. Because phase 2 EADs and RG compete with each other, this type of PVC occurs only at certain $I_{Ca,L}$ ranges in which the EAD amplitude and RG are properly matched.

Modulation of RG-Induced PVCs by Other Factors

We also investigated the effects of other factors on modulating PVC genesis by carrying out simulations that scanned the same parameter space as in Fig. 4*B* under different conditions, and the results are summarized in Fig. 8.

Figure 8*A* shows the case in which we added normal I_{Kr} back into the model (and thus it became the normal control model). The PVC zone was suppressed as expected. It required a much

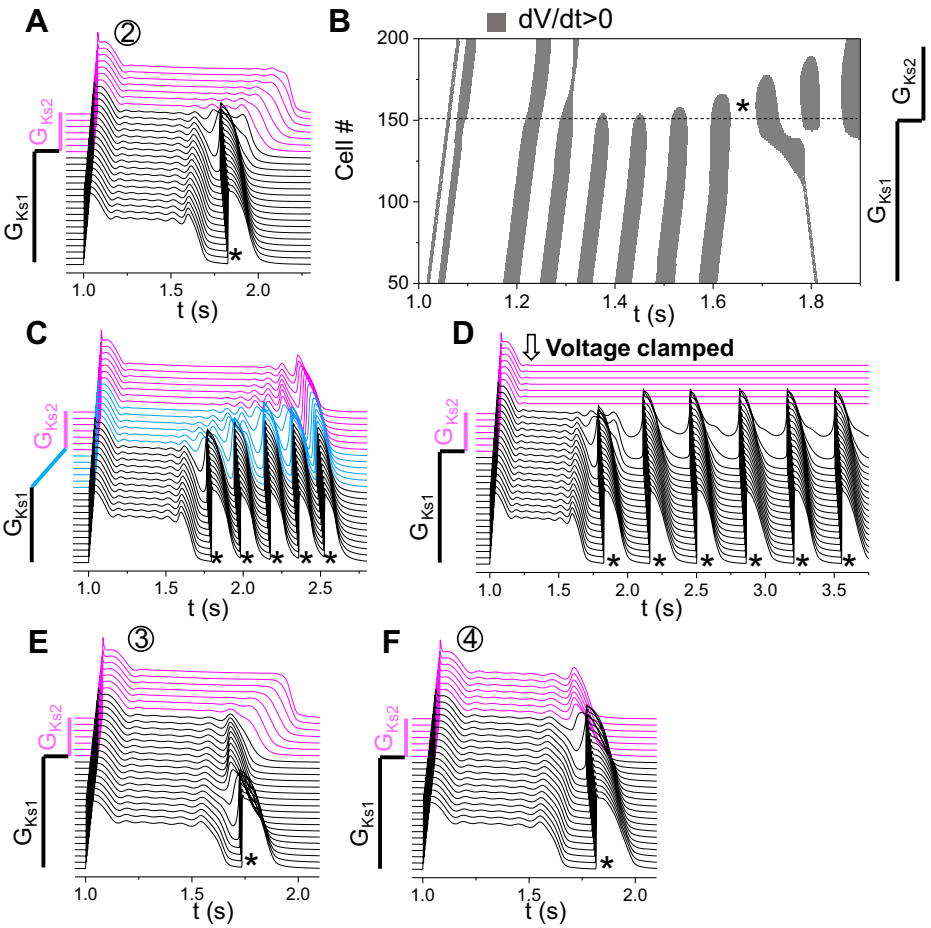

Fig. 7. Small or intermediate RG-induced PVCs. *A*: space-time plot of voltage shown in a PVC (*) generated due to RG via the second mechanism (location "2" in Fig. 4*B*). $G_{Ca,L}$ = 292 mmol/(cm,C) and G_{Ks2} = 0.71 mS/μF. *B*: space-time plot of dV/dt > 0 for the voltage shown in *A*. *C*: same as *A*, but the change of G_{Ks1} to G_{Ks2} occurred across 50 cells. *D*: same as *A*, but the cells in the long APD region were voltage clamped at their values at t = 1,160 ms. *E*: space-time plot of voltage showing a PVC (*) at the boundary ("3" in Fig. 4*B*). $G_{Ca,L}$ = 211 mmol/(cm,C) and G_{Ks2} = 0.71 mS/μF. *F*: space-time plot of voltage showing a PVC (*) when RG is small ("4" in Fig. 4*B*). $G_{Ca,L}$ = 196.75 mmol/(cm,C) and G_{Ks2} = 0.97 mS/μF.

larger $I_{Ca,L}$ or I_{Ks} heterogeneity for PVCs to occur except in some small regions in the upper right quadrant.

Figure 8*B* shows the case in which we reduced gap junction coupling by 50%. This reduction of gap junction coupling had almost no effect on the large RG-induced PVCs but slightly potentiated the boundary effect-induced PVCs (see the changes in the horizontal bar in Fig. 8*B*). This indicates that PVC formation caused by the tissue-scale dynamical instabilities does not depend on cell coupling. This is different from PVCs originating from cellular EAD propagation, whose formation depends sensitively on cell coupling (66).

Because PVC propagation depends on Na current (I_{Na}), we then reduced I_{Na} to investigate its effects on PVC formation in our model. Figure 8*C* shows a case in which we reduced peak I_{Na} by reducing its maximum conductance from 12 to 8 mS/cm^2. This reduction in peak I_{Na} did not reduce PVC formation but instead caused the boundary effect-induced PVCs to occur at a lower $I_{Ca,L}$.

It is well known that hypokalemia potentiates arrhythmia risk in LQTS (12, 46). We lowered the extracellular K concentration ($[K]_o$) from 5.4 (normal) to 2.7 mM to simulate hypokalemia (Fig. 8*D*). This change increased PVCs from both mechanisms but had a much larger effect on small RG- or boundary effect-induced PVCs. Note that more horizontal PVC zones occurred at lower $I_{Ca,L}$. Because our current model lacks Ca/calmodulin-dependent protein kinase II signaling (39), the major effect of lowering $[K]_o$ in our model was inward-rectifier K current (I_{K1}) reduction. Reducing I_{K1} causes a slower phase 3 repolarization and thus promotes phase 3 EAD formation. Therefore, based on our observations shown in Fig. 4, *D* and *E*, these phase 3 EADs can result in PVCs under large RG or $I_{Ca,L}$. When we reduced I_{K1} by the same extent as that (~30%) by lowering $[K]_o$, it had a very similar effect on PVC formation (Fig. 8*E*).

Previous studies have shown that reducing window $I_{Ca,L}$ can eliminate EADs and shorten APD at slow heart rates (29, 30, 40). Figure 8*F* shows the effects of reducing window $I_{Ca,L}$ (by shifting the steady-state inactivation curve to more negative voltages) on PVC formation. Reducing the window $I_{Ca,L}$ could also effectively suppress PVCs of all mechanisms. Note that, in the cases shown in Figs. 8, *B–D*, and 4*B*, PVCs could occur at very small RG (G_{Ks1}~G_{Ks2}). After reducing the window $I_{Ca,L}$, a certain RG was required for PVCs to occur (the PVC zone shifted to the left).

Population-Based Modeling Simulating the Effects of Heterogeneity Diversity

In all the simulations above, the repolarization heterogeneity was simulated by heterogeneous I_{Ks} distributions alone. In real tissue, other ionic currents are also heterogeneously distributed. Moreover, their distributions may vary from cell to cell in the same heart or from heart to heart. To take into account this diversity, population-based models are needed (4, 33, 49, 51).

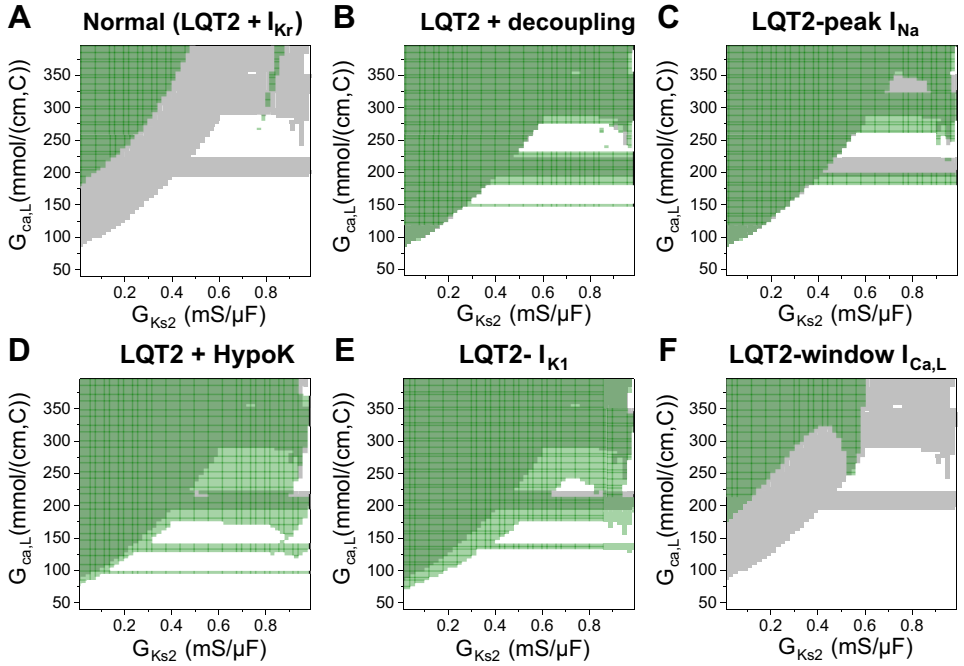

Fig. 8. PVC genesis modulated by other factors. In each panel, the PVC zone in Fig. 4*B* was taken as control and colored gray. The PVC zone after a parameter change was colored green. Because the green was set to be semitransparent, the color became darker when the PVC zone overlapped with that of the control. *A*: normal [LQT2 + the rapid component of the delayed-rectifier potassium current (I_{Kr})]. *B*: reduced gap junction coupling (from 0.0005 to 0.0001 ms/cm^2). *C*: reduced peak Na current (I_{Na}) by reducing the maximum conductance (from 12 to 8 mS/μF). *D*: hypokalemia [extracellular K concentration ($[K]_o$) changed from 5.4 to 2.7 mM]. *E*: reduction of inward-rectifier K current (I_{K1}) by 30% (approximately the same reduction of I_{K1} as in *D*). *F*: 10-mV shift to more negative voltages of the steady-state inactivation curve [f_∞ in the L-type Ca channel (LCC) model] to suppress window $I_{Ca,L}$.

We simulated a population of 1D cables that exhibit a diversity of parameter combinations and APD gradients. The parameters were randomly selected from preassigned ranges (see the legend for Fig. 9). The maximum conductances of I_{Ks}, $I_{Ca,L}$, and I_{to} were heterogeneous in the cable, and those of other currents were homogeneous throughout the cable. The cable length was 200 cells, and the long and short APD regions each contained 100 cells. In each cable, two different conductances of I_{Ks}, $I_{Ca,L}$, or I_{to} were randomly drawn from certain intervals and assigned to the long and short APD regions, respectively.

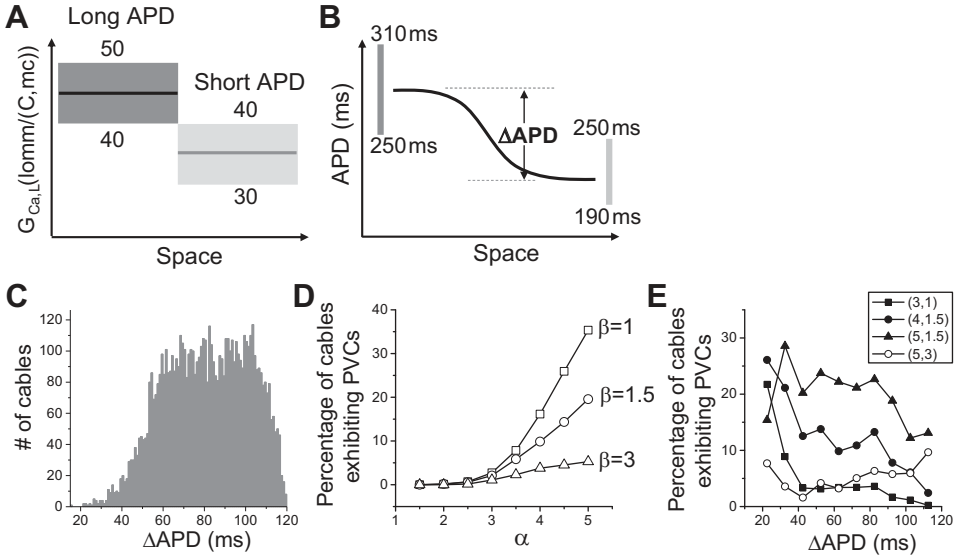

Fig. 9. Population-based analysis of PVC genesis. *A*: schematic plot of the assigned $G_{Ca,L}$ ranges and heterogeneity in the 1D cable model in which two $G_{Ca,L}$ values randomly drawn from the assigned ranges were used for each cable. The cable length was 200 cells, and the long and short APD regions were each 100 cells. We assigned the $G_{Ca,L}$ range from 40 to 50 mmol/(cm,C) in the long APD region and 30 to 40 mmol/(cm,C) in the short APD region. The same two-region heterogeneity was used for the slow transient outward K current ($I_{to,s}$), the fast transient outward K current ($I_{to,f}$), and I_{Ks} with the following assigned maximum conductance ranges (in the same units as in the original model): slow transient outward conductance ($G_{to,s}$, 0.01, 0.04), fast transient outward conductance ($G_{to,f}$, 0.01, 0.11), and G_{Ks} (0.3, 0.7) in the long APD region; and $G_{to,s}$ (0.04, 0.08), $G_{to,f}$ (0.11, 0.22), and G_{Ks} (0.7, 1.3) in the short APD region. I_{K1}, Na/Ca exchange current (I_{NCX}), and I_{NaK} are uniform in space with the following assigned maximum conductance ranges: G_{K1} (0.1, 0.5), Na/Ca exchange conductance (G_{NCX}, 0.5, 1), and maximum conductance of I_{Ks} (G_{NaK}, 1.0, 2.0). *B*: schematic plot of the assigned APD ranges in the 1D cable model. The solid line represents an APD distribution of a specific cable, and ΔAPD was defined as the maximum APD less the minimum APD in this cable. The two vertical bars indicate the allowed APD ranges for the maximum APD and minimum APD, respectively. *C*: histogram of ΔAPD from the 6,000 cables satisfying the APD requirements described in *B*. *D*: percentage of cables exhibiting spontaneous PVCs at different levels of the isoproterenol effects described by α and β. α is the multiplier of $I_{Ca,L}$, and β is the multiplier of I_{Ks}. *E*: percentage of cables exhibiting spontaneous PVCs vs. the initial ΔAPD before isoproterenol (α = β = 1, the same ΔAPD data presented in *C*) for different combinations of α and β as indicated by different symbols.

For example, the $G_{Ca,L}$ range is 40–50 mmol/(cm,C) in the long APD region and 30–40 mmol/(cm,C) in the short APD region (Fig. 9*A*). This gives rise to an ~30% difference in average $I_{Ca,L}$, agreeing with the experimental data by Sims et al. (57). We also applied another constraint based on experimental data from rabbits (6, 26) showing that the maximum APD in the long APD region is 250–310 ms and in the short APD region 190–250 ms (Fig. 9*B*). If the resulting APD of a parameter set fell outside the assigned APD ranges, the case was discarded. Using this filtering method, we generated ~6,000 1D cables that satisfied the APD requirements. Figure 9*C* shows the histogram of ΔAPD as defined in Fig. 9*B*. No PVCs were seen under the control conditions. To induce PVCs and simulate the effects of isoproterenol, we multiplied $I_{Ca,L}$ by a factor α and I_{Ks} by a factor β. Figure 9*D* shows the percentage of the cables exhibiting PVCs under isoproterenol simulated by different combinations of α and β. No PVCs occurred when α was increased less than twofold in the ~6,000 cables for different β. The probability of PVC increased with α after α was increased by twofold or more and became smaller for a larger β. We did not observe a clear correlation between the PVC probability and the ΔAPD at control (Fig. 9*E*), agreeing with our observation that PVCs can occur at both large and small RG.

Pause-Induced Arrhythmias in LQT2

It is widely known that arrhythmias in LQT2 patients tend to occur after a pause (or so-called short-long-short cycle) or under bradycardia (14, 44, 54, 63). It was also demonstrated in transgenic LQT2 rabbits (38). A pause can have two consequences: causing EADs (64) and increasing RG due to different regional rate dependence of APD (43). To demonstrate whether the above mechanisms of PVC genesis are applicable to arrhythmogenesis clinically, we carried out simulations to mimic pause-induced arrhythmias. We paced the 1D cable periodically at 600-ms intervals for many beats and then applied a last pacing stimulation with a coupling interval of 1,500 ms to simulate the pause. Figure 10*A* shows a case in which the RG was large (the same parameters as for Fig. 6*A*), EADs occurred in the long APD region during regular pacing, but no PVCs were induced. After the pause, the APD was increased in both the long and short APD regions, but to a much greater extent in the long APD region. Moreover, EADs in the APD region disappeared after the pause. For the intermediate RG (the same parameters as for Fig. 7*A*), similar behaviors were observed (Fig. 10*B*). For small RG (the same parameters as for Fig. 7*F*), no EADs occurred during the regular pacing but did occur after the pause, and the last EAD in the long APD region elicited the PVC (Fig. 10*C*).

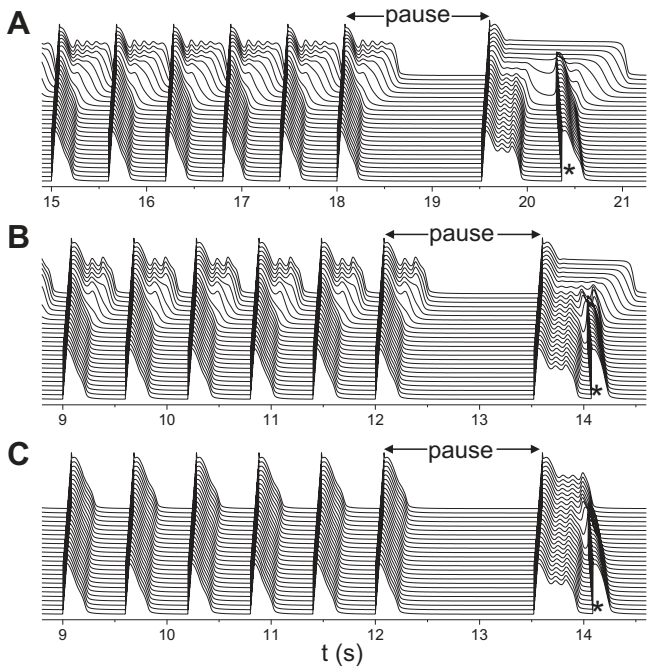

Fig. 10. Pause-induced arrhythmias. Space-time plots of voltage showing pause-induced PVCs (*). The same heterogeneous cable as in Fig. 4*B* was used with G_{Ks1} = 1 mS/μF. *A*: large RG. $G_{Ca,L}$ = 152 mmol/(cm,C) and G_{Ks2} = 0.27 mS/μF. *B*: intermediate RG. $G_{Ca,L}$ = 176 mmol/(cm,C) and G_{Ks2} = 0.45 mS/μF. *C*: small RG. $G_{Ca,L}$ = 176 mmol/(cm,C) and G_{Ks2} = 0.93 mS/μF. The cable was paced at 600 ms for 30 beats in *A* and 20 beats in *B* and *C* followed by a last pacing stimulation that was applied at a coupling interval of 1,500 ms.

DISCUSSION

Here we systematically investigated the mechanisms of spontaneous arrhythmia initiation by RG and the role of phase 2 EADs in LQTS. In transgenic rabbit experiments, we showed that focal excitations tended to occur at spatially steep repolarization gradient regions and propagate unidirectionally. In computer simulation, we showed that cellular phase 2 EADs were mostly suppressed or confined regionally by RG, while tissue-scale phase 3 EADs were induced by RG and $I_{Ca,L}$ to initiate unidirectionally propagating PVCs. Two mechanisms of PVC genesis were identified: *1*) large RG-induced PVCs, in which a critical RG is necessary (Fig. 6); and *2*) small RG-induced PVCs, in which a critical RG is not needed, but the cells in the short APD region need to be prone to cellular EADs, and the presence of phase 2 EADs in the long APD region provides an additional electrical source for PVC formation (Fig. 7). For both mechanisms, $I_{Ca,L}$ plays a critical role, which required severalfold higher $I_{Ca,L}$ than that needed for EADs to occur in a single cell. Because the PVCs are generated from the APD gradient region, propagating unidirectionally, they can initiate reentry without an additional vulnerable substrate, i.e., the triggers and vulnerable substrates of arrhythmias originate from the same source: tissue-scale dynamical instabilities caused by RG and $I_{Ca,L}$. The computer simulations dissected out the roles of EADs and RG in arrhythmogenesis in LQTS and provided mechanistic insights into experimental and clinical observations, as well as potential antiarrhythmic targets for LQTS, as discussed below.

Roles of EADs and RG in Arrhythmogenesis in LQTS

EADs, as a hallmark of LQTS, are widely considered triggers of TdP. As shown in many experimental (20, 26, 59) and computational (10, 11, 35) studies in isolated ventricular myocytes, ionic current defects in LQTS cause mainly phase 2 EADs. Computer simulation studies demonstrated that phase 3 EADs can propagate to generate PVCs when there is a sufficient electrical source (66), and phase 2 EADs might produce PVCs in heterogeneous tissue when the cells are very weakly coupled to simulate ischemia (15, 50). However, no studies

have shown that phase 2 EADs can induce PVCs in LQTS in which gap junction coupling is normal. Our simulations showed that the cellular phase 2 EADs were suppressed or confined regionally by RG, no matter how large the EAD area was, which was not affected by severalfold reduction of gap junction coupling (see Fig. 5). Moreover, the comparison of parameter regions of cellular phase 2 EADs and PVCs in tissue showed little correlations (Fig. 4, *A* and *B*). Although cellular phase 2 EADs may not directly initiate PVCs, they still play important roles in arrhythmogenesis in LQTS. First, when the RG is very small or at the tissue boundary, a phase 2 EAD can survive in the APD gradient region and provide an additional electrical source for PVC formation. Second, for PVCs initiated by small or intermediate RGs, the cells in the short APD region must be prone to cellular EADs, and thus a small electrical source from their neighbors can cause tissue-scale phase 2 and phase 3 EADs to induce PVCs.

RG exists in normal hearts and is increased in LQTS (6, 62). It is widely assumed that EADs are the sources of PVCs and that increased RG promotes a vulnerable substrate for conduction block to cause reentry. However, this picture of arrhythmogenesis in LQTS may not be true. First, increased RG tends to suppress EADs due to the source-sink effect as also shown in our simulations (Fig. 5), while spontaneous arrhythmias required a critical RG (67, 68). Second, in both previous optical mapping studies in drug-induced LQTS (23, 27, 32) and the current study of transgenic LQT2, ectopic excitations tend to occur in the steep RG region and propagate unidirectionally. If a cellular phase 2 EAD were the cause of an ectopic beat, the earliest activation site would be in the long APD region instead of the RG region, since phase 2 EADs are more suppressed in the RG region. Our simulations show that tissue-scale phase 3 EADs and PVCs are caused by RG, which originate from the steep RG region and propagate unidirectionally. The presence of the cellular EADs is not required but can potentiate PVC formation. The tissue-scale EADs and PVCs are the result of a tissue-scale dynamical instability that relies on both RG and the properties of the ionic currents, while the instability causing cellular EADs relies solely on the properties of the ionic currents (42). The cellular factors promoting cellular EADs also promote tissue-scale EADs and PVCs under increased RG, but the tissue-scale EAD and PVC formation requires a much larger $I_{Ca,L}$. This explains why both cellular EADs and tissue RG are important for arrhythmogenesis in LQTS. Because RG-induced PVCs propagate unidirectionally, promoting both a trigger and a vulnerable substrate at the same location, reentry occurs spontaneously without requiring an additional RG region for conduction block. This is different from the traditional concept that arrhythmia triggers and substrates are due to different causes, which interact to induce arrhythmias (41, 47).

Mechanisms of Focal Excitation in Transgenic Rabbit Hearts

As shown in our experiments in transgenic LQT2 hearts (Fig. 2), focal excitations tend to occur in the steep-RG region and propagate unidiretionally. We observed different focal excitation patterns, which are similar to those in our simulations (Fig. 3). EADs were present in the long APD region, consistent with the previous findings that single cells isolated from the LV of LQT2 rabbit hearts often exhibited EADs (6, 26). According to our computer simulations, PVCs can occur in tissue with small to very large RG, propagating unidirectionally or in all directions in either the presence or absence of cellular phase 2 EADs. We postulate that both mechanisms of PVC genesis identified in computer simulations may occur in LQT2 rabbits. RG-induced ectopic excitations may also be responsible for arrhythmogenesis in transgenic LQT1 rabbits, as shown in our previous experiments (24), which found that the APD is longer in LV than in RV, and ectopic excitations frequently originated from the border region between RV and LV and propagated toward RV but not LV [see Fig. 4 in Kim et al. (24)]. In both transgenic LQT1 and LQT2 hearts, isoproterenol was needed to induce ectopic excitations, indicating that greater $I_{Ca,L}$ was required, which agrees with the computer simulation results.

Role of $I_{Ca,L}$ *in Arrhythmogenesis in LQTS*

An important observation from our simulations in this study is that the magnitude of $I_{Ca,L}$ needed to initiate PVCs or focal excitations in tissue is much larger than either its control value or the magnitude required for the occurrence of EADs in a single cell. Moreover, a smaller RG is needed for a larger $I_{Ca,L}$ to induce PVCs. In our transgenic rabbit experiments, spontaneous arrhythmias were always initiated under isoproterenol. As shown in our computer simulations (Figs. 4*B* and 10*C*), PVCs could occur when RG is relatively small, as long as $I_{Ca,L}$ is strong enough. Isoproterenol can increase $I_{Ca,L}$ by twofold in rabbit myocytes (26), which may be strong enough to promote arrhythmias in LQT2 rabbit hearts. Other studies have shown that progesterone (which decreases $I_{Ca,L}$) is protective while estrogen (which increases $I_{Ca,L}$) is proarrhythmic in LQT2 (37, 57, 69). Clinically, β-blockers, although they slow heart rates, are still the most effective treatment for arrhythmia prevention in LQTS (19, 55). The current experimental and clinical observations agree with the observation that a large $I_{Ca,L}$ is needed for spontaneous arrhythmias in LQTS. Moreover, recent studies have shown that enhanced $I_{Ca,L}$ can mediate conduction in cardiac tissue under reduced repolarization reserve without activation of I_{Na} or in absence of I_{Na} (7, 8, 24, 61).

Although $I_{Ca,L}$ plays a key role in arrhythmogenesis in LQTS, the traditional L-type Ca channel (LCC) blockade cannot be used as an antiarrhythmic therapy, since it also has the negative ionotropic effect of suppressing contraction. Our previous studies showed that reducing window $I_{Ca,L}$ by modifying LCC properties could effectively shorten ultralong APD and suppress EADs (30, 40, 42). Unlike the traditional LCC blockers, reducing window $I_{Ca,L}$ has almost no effect on Ca cycling under normal conditions and thus will have almost no effect on contraction. As shown in our simulations in Fig. 8*F*, suppressing the window $I_{Ca,L}$ without reducing its peak value can still effectively suppress the PVCs caused by the tissue-scale dynamical instabilities. This indicates that modifying the LCC properties that suppress the window $I_{Ca,L}$ could be an effective candidate therapeutic target for suppressing arrhythmias in LQTS.

Limitations

Because the optical mapping only recorded signals from epicardial or subepicardial cells, it cannot be sure that the foci shown in our recordings (Fig. 2) were the true origins of the focal excitations. They could be breakthroughs originating from somewhere underneath the surface. As shown by Yan et al. (67), ectopic beats can be caused by transmural RG, and we believe that the same mechanisms identified in this study are likely responsible. The unidirectional propagation of PVCs observed in our experiments could also be caused or potentiated by other tissue-scale heterogeneity factors, such as the LV-to-RV thickness gradient (3). Another limitation of the experimental study is that, under the normal condition, the cycle lengths of sinus rhythm for the rabbit hearts range from 180 to 350 ms. Under these heart rates, we were not able to observe EADs and PVCs. We ablated the AV node to slow the heart rate to promote EADs and PVCs. However, after the AV ablation, the APD and the patterns of RG may be very different from those under normal conditions, and thus the mechanisms of arrhythmogenesis may not be the same for the two conditions. Nevertheless, our goal is to understand the mechanisms of spontaneous initiation of arrhythmias caused by RG, and the mechanistic insights obtained under the slow heart rates may still provide important insights into spontaneous initiation of ventricular arrhythmias in human.

In the present study, the simulations were carried out in single-cell, 1D cable, and 2D tissue, but real hearts are three-dimensional (3D) with specific geometries. Due to the source-sink and curvature effects, the conditions for PVC formation and reentry induction in 3D tissue may differ from 1D and 2D tissue. In a recent study (60), Vandersickel et al. showed that TdP could be induced spontaneously by RG in 2D tissue, similar to the mechanisms identified in the current study, and they demonstrated that the same mechanism was also responsible for TdP in the anatomically based 3D human ventricle model. Similar 3D human heart simulations were carried out in another recent study by Dutta et al. (15) who showed that spontaneous ectopic excitations and reentrant arrhythmias could be caused by dispersion of repolarization in ischemic tissue with reduced repolarization reserve. However, as shown in this study, PVC formation was caused by tissue-scale dynamical instabilities; the source-sink or curvature effects may not be the same as the traditional source-sink or curvature effects as in the propagation of EADs or delayed afterdepolarizations (66). More rigorous analyses are needed to dissect this out. In all the models we simulated, none generated Ca oscillation-mediated EADs (58, 65, 71), while experimental studies have shown that Ca oscillations may also play an important role in formation of focal excitations in LQTS (9, 23); these may be responsible for the focal exactions observed in our experiments. Additionally, we investigated only the effects of RG caused by preexisting heterogeneities. As we showed previously, in the presence of EADs, chaotic AP dynamics can give rise to dynamical RG (53), which can also promote PVCs via the same mechanisms as shown in this study.

In conclusion, in LQT2 rabbit hearts, cellular phase 2 EADs, which may be either suppressed or regionally confined in heterogeneous tissue, cannot propagate into PVCs. PVCs are a result of tissue-scale dynamical instabilities caused by RG and enhanced $I_{Ca,L}$, differing from that PVCs are a consequence of EAD propagation. Two mechanisms of PVCs can exist. In the first mechanism, occurrence of PVCs requires a critical RG without requiring cellular EADs. In the second mechanism, PVCs can occur in an intermediate or small RG that is potentiated when the cells in the long APD region exhibit EADs or the cells in the short APD region are prone to EADs. Both mechanisms require the presence of a large $I_{Ca,L}$. Because PVC formation requires the occurrence of tissue-scale phase 3 EADs, it sensitively depends on I_{K1} conductance, i.e., reducing I_{K1} conductance or hypokalemia promotes PVCs, agreeing with the knowledge that hypokalemia is a severe risk factor of arrhythmogenesis in LQTS patients. Unlike the case of PVCs originating from EAD propagation (66), gap junction coupling has a small effect on the PVC formation caused by the tissue-scale dynamical instabilities. Because the PVCs induced by the tissue-scale dynamical instabilities propagate unidirectionally, an additional tissue substrate is not required for initiation of reentrant arrhythmias. In other words, the arrhythmia trigger (i.e., PVCs) and vulnerable tissue substrate originate from the same source. The mechanistic insights into PVC formation and arrhythmogenesis from the present study may shed light on identifying novel therapeutic targets for preventing arrhythmias in LQTS.

ACKNOWLEDGMENTS

We thank the members of the arrhythmia groups at UCLA and Rhode Island Hospital for useful comments.

GRANTS

This work is supported by National Heart, Lung, and Blood Institute Grants R01-HL-110791 and R01-HL-096669 (to B.-R. Choi).

DISCLOSURES

No conflicts of interest, financial or otherwise, are declared by the authors.

AUTHOR CONTRIBUTIONS

X.H., B.-R.C., and Z.Q. conception and design of research; X.H. and T.Y.K. performed experiments; X.H., T.Y.K., B.-R.C., and Z.Q. analyzed data; X.H., T.Y.K., G.K., B.-R.C., and Z.Q. interpreted results of experiments; X.H., T.Y.K., and Z.Q. prepared figures; X.H., T.Y.K., B.-R.C., and Z.Q. drafted manuscript; X.H., T.Y.K., G.K., B.-R.C., and Z.Q. edited and revised manuscript; X.H., T.Y.K., G.K., B.-R.C., and Z.Q. approved final version of manuscript.

REFERENCES

1. **Antzelevitch C.** Ionic, molecular, and cellular bases of QT-interval prolongation and torsade de pointes. *Europace* 9, *Suppl* 4: iv4–iv15, 2007.
2. **Antzelevitch C.** Role of transmural dispersion of repolarization in the genesis of drug-induced torsades de pointes. *Heart Rhythm* 2: S9–S15, 2005.
3. **Boyle PM, Park CJ, Arevalo HJ, Vigmond EJ, Trayanova NA.** Sodium current reduction unmasks a structure-dependent substrate for arrhythmogenesis in the normal ventricles. *PLoS ONE* 9: e86947, 2014.
4. **Britton OJ, Bueno-Orovio A, Van Ammel K, Lu HR, Towart R, Gallacher DJ, Rodriguez B.** Experimentally calibrated population of models predicts and explains intersubject variability in cardiac cellular electrophysiology. *Proc Natl Acad Sci USA* 110: E2098–E2105, 2013.
5. **Brugada P, Wellens HJJ.** Early afterdepolarizations: role in conduction block, "prolonged repolarization-dependent reexcitation," and tachyarrhythmias in the human heart. *Pacing Clin Electrophysiol* 8: 889–896, 1985.
6. **Brunner M, Peng X, Liu GX, Ren XQ, Ziv O, Choi BR, Mathur R, Hajjiri M, Odening KE, Steinberg E, Folco EJ, Pringa E, Centracchio J, Macharzina RR, Donahay T, Schofield L, Rana N, Kirk M, Mitchell GF, Poppas A, Zehender M, Koren G.** Mechanisms of cardiac arrhyth-

mias and sudden death in transgenic rabbits with long QT syndrome. *J Clin Invest* 118: 2246–2259, 2008.
7. **Chang MG, de Lange E, Calmettes G, Garfinkel A, Qu Z, Weiss JN.** Pro- and antiarrhythmic effects of ATP-sensitive potassium current activation on reentry during early afterdepolarization-mediated arrhythmias. *Heart Rhythm* 10: 575–582, 2013.
8. **Chang MG, Sato D, de Lange E, Lee JH, Karagueuzian HS, Garfinkel A, Weiss JN, Qu Z.** Bi-stable wave propagation and early afterdepolarization-mediated cardiac arrhythmias. *Heart Rhythm* 9: 115–122, 2012.
9. **Choi BR, Burton F, Salama G.** Cytosolic Ca2+ triggers early afterdepolarizations and Torsade de Pointes in rabbit hearts with type 2 long QT syndrome. *J Physiol Lond* 543: 615–631, 2002.
10. **Clancy CE, Rudy Y.** Cellular consequences of HERG mutations in the long QT syndrome: precursors to sudden cardiac death. *Cardiovasc Res* 50: 301–313, 2001.
11. **Clancy CE, Rudy Y.** Linking a genetic defect to its cellular phenotype in a cardiac arrhythmia. *Nature* 400: 566–569, 1999.
12. **Cohen JD, Neaton JD, Prineas RJ, Daniels KA.** Diuretics, serum potassium and ventricular arrhythmias in the Multiple Risk Factor Intervention Trial. *Am J Cardiol* 60: 548–554, 1987.
13. **Damiano BP, Rosen MR.** Effects of pacing on triggered activity induced by early afterdepolarizations. *Circulation* 69: 1013–1025, 1984.
14. **Dessertenne F.** Ventricular tachycardia with 2 variable opposing foci (translated from French). *Arch Mal Coeur Vaiss* 59: 263–272, 1966.
15. **Dutta S, Mincholé A, Zacur E, Quinn TA, Taggart P, Rodriguez B.** Early afterdepolarizations promote transmural reentry in ischemic human ventricles with reduced repolarization reserve. *Prog Biophys Mol Biol* 120: 236–248, 2016.
16. **El-Sherif N, Craelius W, Boutjdir M, Gough WB.** Early afterdepolarizations and arrhythmogenesis. *J Cardiovasc Electrophysiol* 1: 145–160, 1990.
17. **El-Sherif N, Turitto G.** The Long QT syndrome and Torsade De Pointes. *Pacing Clin Electrophysiol* 22: 91–110, 1999.
18. **Gintant GA.** Regional differences in IK density in canine left ventricle: role of IK,s in electrical heterogeneity. *Am J Physiol Heart Circ Physiol* 268: H604–H613, 1995.
19. **Goldenberg I, Bradley J, Moss A, McNitt S, Polonsky S, Robinson JL, Andrews M, Zareba W, International LQTS Registry Investigators.** Beta-blocker efficacy in high-risk patients with the congenital long-QT syndrome types 1 and 2: implications for Patient Management. *J Cardiovasc Electrophysiol* 21: 893–901, 2010.
20. **Guo D, Zhao X, Wu Y, Liu T, Kowey PR, Yan GX.** L-type calcium current reactivation contributes to arrhythmogenesis associated with action potential triangulation. *J Cardiovasc Electrophysiol* 18: 196–203, 2007.
21. **Gupta P, Patel C, Patel H, Narayanaswamy S, Malhotra B, Green JT, Yan GX.** T(p-e)/QT ratio as an index of arrhythmogenesis. *J Electrocardiol* 41: 567–574, 2008.
22. **Huelsing DJ, Spitzer KW, Pollard AE.** Electrotonic suppression of early afterdepolarizations in isolated rabbit Purkinje myocytes. *Am J Physiol Heart Circ Physiol* 279: H250–H259, 2000.
23. **Kim JJ, Němec J, Li Q, Salama G.** Synchronous systolic subcellular ca2+-elevations underlie ventricular arrhythmia in drug-induced long QT type 2. *Circulation* 8: 703–712, 2015.
24. **Kim TY, Kunitomo Y, Pfeiffer Z, Patel D, Hwang J, Harrison K, Patel B, Jeng P, Ziv O, Lu Y, Peng X, Qu Z, Koren G, Choi BR.** Complex excitation dynamics underlie polymorphic ventricular tachycardia in a transgenic rabbit model of long QT syndrome type 1. *Heart Rhythm* 12: 220–228, 2015.
25. **Li Y, Lu ZY, Xiao JM, Ma J, Niu HY, Liu N, Ruan YF.** Effect of imidapril on heterogeneity of slow component of delayed rectifying K^+ current in rabbit left ventricular hypertrophic myocytes. *Acta Pharmacologica Sinica* 24: 681–686, 2003.
26. **Liu GX, Choi BR, Ziv O, Li W, de Lange E, Qu Z, Koren G.** Differential conditions for early after-depolarizations and triggered activity in cardiomyocytes derived from transgenic LQT1 and LQT2 rabbits. *J Physiol* 590: 1171–1180, 2012.
27. **Liu J, Laurita KR.** The mechanism of pause-induced torsade de pointes in long QT syndrome. *J Cardiovasc Electrophysiol* 16: 981–987, 2005.
28. **Luo CH, Rudy Y.** A dynamical model of the cardiac ventricular action potential: I. simulations of ionic currents and concentration changes. *Circ Res* 74: 1071–1096, 1994.
29. **Madhvani RV, Angelini M, Xie Y, Pantazis A, Suriany S, Borgstrom NP, Garfinkel A, Qu Z, Weiss JN, Olcese R.** Targeting the late component of the cardiac L-type Ca2+ current to suppress early afterdepolarizations. *J Gen Physiol* 145: 395–404, 2015.
30. **Madhvani RV, Xie Y, Pantazis A, Garfinkel A, Qu Z, Weiss JN, Olcese R.** Shaping a new Ca(2+) conductance to suppress early afterdepolarizations in cardiac myocytes. *J Physiol* 589: 6081–6092, 2011.
31. **Mahajan A, Shiferaw Y, Sato D, Baher A, Olcese R, Xie LH, Yang MJ, Chen PS, Restrepo JG, Karma A, Garfinkel A, Qu Z, Weiss JN.** A rabbit ventricular action potential model replicating cardiac dynamics at rapid heart rates. *Biophys J* 94: 392–410, 2008.
32. **Maruyama M, Lin SF, Xie Y, Chua SK, Joung B, Han S, Shinohara T, Shen MJ, Qu Z, Weiss JN, Chen PS.** Genesis of phase 3 early afterdepolarizations and triggered activity in acquired long-QT syndrome. *Circ Arrhythm Electrophysiol* 4: 103–111, 2011.
33. **Muszkiewicz A, Britton OJ, Gemmell P, Passini E, Sánchez C, Zhou X, Carusi A, Quinn TA, Burrage K, Bueno-Orovio A, Rodriguez B.** Variability in cardiac electrophysiology: Using experimentally-calibrated populations of models to move beyond the single virtual physiological human paradigm. *Prog Biophys Mol Biol* 120: 115–127, 2016.
34. **Napolitano C, Bloise R, Monteforte N, Priori SG.** Sudden cardiac death and genetic ion channelopathies. *Circulation* 125: 2027–2034, 2012.
35. **O'Hara T, Rudy Y.** Quantitative comparison of cardiac ventricular myocyte electrophysiology and response to drugs in human and nonhuman species. *Am J Physiol Heart Circ Physiol* 302: H1023–H1030, 2012.
36. **O'Hara T, Virag L, Varro A, Rudy Y.** Simulation of the undiseased human cardiac ventricular action potential: model formulation and experimental validation. *PLoS Comput Biol* 7: e1002061, 2011.
37. **Odening KE, Choi BR, Koren G.** Sex hormones and cardiac arrest in long QT syndrome: does progesterone represent a potential new antiarrhythmic therapy? *Heart Rhythm* 9: 1150–1152, 2012.
38. **Odening KE, Choi BR, Liu GX, Hartmann K, Ziv O, Chaves L, Schofield L, Centracchio J, Zehender M, Peng X, Brunner M, Koren G.** Estradiol promotes sudden cardiac death in transgenic long QT type 2 rabbits while progesterone is protective. *Heart Rhythm* 9: 823–832, 2012.
39. **Pezhouman A, Singh N, Song Z, Nivala M, Eskandari A, Cao H, Bapat A, Ko CY, Nguyen TP, Qu Z, Karagueuzian HS, Weiss JN.** Molecular basis of hypokalemia-induced ventricular fibrillation. *Circulation* 132: 1528–1537, 2015.
40. **Qu Z, Chung D.** Mechanisms and determinants of ultralong action potential duration and slow rate-dependence in cardiac myocytes. *PLoS One* 7: e43587, 2012.
41. **Qu Z, Weiss JN.** Mechanisms of ventricular arrhythmias: from molecular fluctuations to electrical turbulence. *Annu Rev Physiol* 77: 29–55, 2015.
42. **Qu Z, Xie LH, Olcese R, Karagueuzian HS, Chen PS, Garfinkel A, Weiss JN.** Early afterdepolarizations in cardiac myocytes: beyond reduced repolarization reserve. *Cardiovasc Res* 99: 6–15, 2013.
43. **Restivo M, Caref EB, Kozhevnikov DO, El-Sherif N.** Spatial dispersion of repolarization is a key factor in the arrhythmogenicity of long QT syndrome. *J Cardiovasc Electrophysiol* 15: 323–331, 2004.
44. **Roden DM, Anderson ME.** The pause that refreshes, or does it? Mechanisms in torsades de pointes. *Heart* 84: 235–237, 2000.
45. **Roden DM, Lazzara R, Rosen M, Schwartz PJ, Towbin J, Vincent M.** Multiple mechanisms in the long-QT syndrome: current knowledge, gaps, and future directions. *Circulation* 94: 1996–2012, 1996.
46. **Roden DM, Woosley RL, Primm RK.** Incidence and clinical features of the quinidine-associated long QT syndrome: Implications for patient care. *Am Heart J* 111: 1088–1093, 1986.
47. **Rosen MR.** Mechanisms for arrhythmias. *Am J Cardiol* 61: 2A–8A, 1988.
48. **Rush S, Larsen H.** A practical algorithm for solving dynamic membrane equations. *IEEE Trans Biomed Eng* 25: 389–392, 1978.
49. **Sadrieh A, Domanski L, Pitt-Francis J, Mann SA, Hodkinson EC, Ng CA, Perry MD, Taylor JA, Gavaghan D, Subbiah RN, Vandenberg JI, Hill AP.** Multiscale cardiac modelling reveals the origins of notched T waves in long QT syndrome type 2. *Nat Commun* 5: 5069, 2014.
50. **Saiz J, Ferrero JM Jr, Monserrat M, Ferrero JM, Thakor NV.** Influence of electrical coupling on early afterdepolarizations in ventricular myocytes. *IEEE Trans Biomed Eng* 46: 138–147, 1999.
51. **Sarkar AX, Sobie EA.** Quantification of repolarization reserve to understand interpatient variability in the response to proarrhythmic drugs: a computational analysis. *Heart Rhythm* 8: 1749–1755, 2011.
52. **Sato D, Xie LH, Nguyen TP, Weiss JN, Qu Z.** Irregularly appearing early afterdepolarizations in cardiac myocytes: random fluctuations or dynamical chaos? *Biophys J* 99: 765–773, 2010.
53. **Sato D, Xie LH, Sovari AA, Tran DX, Morita N, Xie F, Karagueuzian H, Garfinkel A, Weiss JN, Qu Z.** Synchronization of chaotic early

afterdepolarizations in the genesis of cardiac arrhythmias. *Proc Natl Acad Sci USA* 106: 2983–2988, 2009.
54. **Schwartz PJ.** The congenital long QT syndromes from genotype to phenotype: clinical implications. *J Intern Med* 259: 39–47, 2006.
55. **Schwartz PJ, Ackerman MJ.** The long QT syndrome: a transatlantic clinical approach to diagnosis and therapy. *Eur Heart J* 34: 3109–3116, 2013.
56. **Shimizu W, Antzelevitch C.** Differential effects of beta-adrenergic agonists and antagonists in LQT1, LQT2 and LQT3 models of the long QT syndrome. *J Am Coll Cardiol* 35: 778–786, 2000.
57. **Sims C, Reisenweber S, Viswanathan PC, Choi BR, Walker WH, Salama G.** Sex, age, and regional differences in L-type calcium current are important determinants of arrhythmia phenotype in rabbit hearts with drug-induced long QT type 2. *Circ Res* 102: e86–e100, 2008.
58. **Song Z, Ko CY, Nivala M, Weiss James N, Qu Z.** Calcium-Voltage Coupling in the Genesis of Early and Delayed Afterdepolarizations in Cardiac Myocytes. *Biophys J* 108: 1908–1921, 2015.
59. **Terentyev D, Rees CM, Li W, Cooper LL, Jindal HK, Peng X, Lu Y, Terentyeva R, Odening KE, Daley J, Bist K, Choi BR, Karma A, Koren G.** Hyperphosphorylation of RyRs underlies triggered activity in transgenic rabbit model of LQT2 syndrome. *Circ Res* 115: 919–928, 2014.
60. **Vandersickel N, de Boer TP, Vos MA, Panfilov AV.** Perpetuation of torsade de pointes in heterogeneous hearts: competing foci or re-entry? *J Physiol* In press.
61. **Vandersickel N, Kazbanov IV, Nuitermans A, Weise LD, Pandit R, Panfilov AV.** A study of early afterdepolarizations in a model for human ventricular tissue. *PLoS ONE* 9: e84595, 2014.
62. **Vijayakumar R, Silva JNA, Desouza KA, Abraham RL, Strom M, Sacher F, Van Hare GF, Haïssaguerre M, Roden DM, Rudy Y.** Electrophysiologic substrate in congenital long qt syndrome: noninvasive mapping with electrocardiographic imaging (ECGI). *Circulation* 130: 1936–1943, 2014.
63. **Viskin S, Fish R, Zeltser D, Belhassen B, Heller K, Brosh D, Laniado S, Barron HV.** Arrhythmias in the congenital long QT syndrome: how often is torsade de pointes pause dependent? *Heart* 83: 661–666, 2000.
64. **Viswanathan PC, Rudy Y.** Pause induced early afterdepolarizations in the long QT syndrome: a simulation study. *Cardiovasc Res* 42: 530–542, 1999.
65. **Volders PG, Kulcsar A, Vos MA, Sipido KR, Wellens HJ, Lazzara R, Szabo B.** Similarities between early and delayed afterdepolarizations induced by isoproterenol in canine ventricular myocytes. *Cardiovasc Res* 34: 348–359, 1997.
66. **Xie Y, Sato D, Garfinkel A, Qu Z, Weiss JN.** So little source, so much sink: requirements for afterdepolarizations to propagate in tissue. *Biophys J* 99: 1408–1415, 2010.
67. **Yan GX, Wu Y, Liu T, Wang J, Marinchak RA, Kowey PR.** Phase 2 Early afterdepolarization as a trigger of polymorphic ventricular tachycardia in acquired long-QT syndrome: direct evidence from intracellular recordings in the intact left ventricular wall. *Circulation* 103: 2851–2856, 2001.
68. **Yan GX, Antzelevitch C.** Cellular basis for the normal T wave and the electrocardiographic manifestations of the long-QT syndrome. *Circulation* 98: 1928–1936, 1998.
69. **Yang X, Chen G, Papp R, Defranco DB, Zeng F, Salama G.** Oestrogen upregulates L-type Ca(2)(+) channels via oestrogen-receptor- by a regional genomic mechanism in female rabbit hearts. *J Physiol* 590: 493–508, 2012.
70. **Zeng J, Laurita KR, Rosenbaum DS, Rudy Y.** Two components of the delayed rectifier K+ current in ventricular myocytes of the guinea pig type. Theoretical formulation and their role in repolarization. *Circ Res* 77: 140–152, 1995.
71. **Zhao Z, Wen H, Fefelova N, Allen C, Baba A, Matsuda T, Xie LH.** Revisiting the ionic mechanisms of early afterdepolarizations in cardiomyocytes: predominant by Ca waves or Ca currents? *Am J Physiol Heart Circ Physiol* 302: H1636–H1644, 2012.
72. **Ziv O, Morales E, Song YK, Peng X, Odening KE, Buxton AE, Karma A, Koren G, Choi BR.** Origin of complex behaviour of spatially discordant alternans in a transgenic rabbit model of type 2 long QT syndrome. *J Physiol* 587: 4661–4680, 2009.